

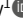
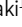






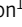
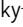
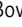


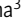



ARTICLE

Microglia at sites of atrophy restrict the progression of retinal degeneration via galectin-3 and Trem2

Chen Yu¹ , Eleonora M. Lad¹ , Rose Mathew¹ , Nobuhiko Shiraki¹ , Sejiro Littleton^{1,2} , Yun Chen^{3,4} , Jinchao Hou^{3,4} , Kai Schlepckow⁵ , Simone Degan¹ , Lindsey Chew¹ , Joshua Amason¹ , Joan Kalnitsky¹ , Catherine Bowes Rickman^{1,6} , Alan D. Proia^{1,7,8} , Marco Colonna³ , Christian Haass^{5,9,10} , and Daniel R. Saban^{1,2} 

Outer retinal degenerations, including age-related macular degeneration (AMD), are characterized by photoreceptor and retinal pigment epithelium (RPE) atrophy. In these blinding diseases, macrophages accumulate at atrophic sites, but their ontogeny and niche specialization remain poorly understood, especially in humans. We uncovered a unique profile of microglia, marked by galectin-3 upregulation, at atrophic sites in mouse models of retinal degeneration and human AMD. In disease models, conditional deletion of galectin-3 in microglia led to phagocytosis defects and consequent augmented photoreceptor death, RPE damage, and vision loss, indicating protective roles. Mechanistically, Trem2 signaling orchestrated microglial migration to atrophic sites and induced galectin-3 expression. Moreover, pharmacologic Trem2 agonization led to heightened protection but in a galectin-3–dependent manner. In elderly human subjects, we identified this highly conserved microglial population that expressed galectin-3 and Trem2. This population was significantly enriched in the macular RPE-choroid of AMD subjects. Collectively, our findings reveal a neuroprotective population of microglia and a potential therapeutic target for mitigating retinal degeneration.

Introduction

Microglia, the resident macrophages of the central nervous system (CNS; Ajami et al., 2007; Butovsky et al., 2014; Buttgerit et al., 2016; Ginhoux et al., 2010; Mildner et al., 2007), are highly specialized to respective microenvironments such that their functionality can vary by location and pathological perturbation, as shown in the retina and elsewhere in the CNS (Badimon et al., 2020; De Biase et al., 2017; Grabert et al., 2016; Kana et al., 2019; O’Koren et al., 2019). This distinctive adaptability is pertinent in neurodegenerative states as well, where microglia migrate to the area of CNS pathology and alter their molecular and functional profiles (Keren-Shaul et al., 2017; Krasemann et al., 2017; O’Koren et al., 2019; Yamasaki et al., 2014). There is also an intrinsic microglial contribution in producing these changes (Bennett et al., 2018; Reed-Geaghan et al., 2020; Shemer et al., 2018) since infiltrated monocyte-derived macrophages do not fully adopt the same characteristics (Ajami et al., 2011; Cronk et al., 2018; O’Koren et al., 2016; Prokop et al., 2015; Varvel et al., 2015). Hence, both ontogeny and location are critical

factors in understanding microglial roles in neurodegenerative diseases.

Degenerative diseases of the outer retina, including age-related macular degeneration (AMD), are common causes of blindness in adults and are characterized by retinal atrophy of photoreceptors and retinal pigment epithelium (RPE). AMD alone afflicts ~196 million worldwide (Wong et al., 2014), yet only 10% of these cases are treatable, highlighting a major unmet medical need (Rashid et al., 2019). Innate immunity is deemed important in AMD pathobiology (Doyle et al., 2012; Hageman et al., 2001; Kerur et al., 2018; Tarallo et al., 2012), and the major genetic risk genes for AMD (Fritsche et al., 2016), including *CFH*, *ARMS2-HTRA1*, *APOE*, and *C3*, are all expressed by or impact the immune system (Beguier et al., 2020; Calippe et al., 2017; Levy et al., 2015; Silverman et al., 2019). Significant for these diseases, macrophages migrate and accumulate ectopically in the subretinal space, the area within the sites of atrophy (Combadière et al., 2007; Greferath et al., 2016; Gupta

¹Department of Ophthalmology, Duke University School of Medicine, Durham, NC, USA; ²Department of Immunology, Duke University, Durham, NC, USA; ³Department of Pathology and Immunology, Washington University School of Medicine, St. Louis, MO, USA; ⁴Department of Neurology, Washington University School of Medicine, St. Louis, MO, USA; ⁵German Center for Neurodegenerative Diseases Munich, Munich, Germany; ⁶Department of Cell Biology, Duke University, Durham, NC, USA; ⁷Department of Pathology, Duke University School of Medicine, Durham, NC, USA; ⁸Department of Pathology, Campbell University Jerry M. Wallace School of Osteopathic Medicine, Lillington, NC, USA; ⁹Chair of Metabolic Biochemistry, Faculty of Medicine, Biomedical Center, Ludwig-Maximilians-Universität München, Munich, Germany; ¹⁰Munich Cluster for Systems Neurology (SyNergy), Munich, Germany.

Correspondence to Daniel R. Saban: daniel.saban@duke.edu.

© 2024 Yu et al. This article is distributed under the terms of an Attribution–Noncommercial–Share Alike–No Mirror Sites license for the first six months after the publication date (see <http://www.rupress.org/terms/>). After six months it is available under a Creative Commons License (Attribution–Noncommercial–Share Alike 4.0 International license, as described at <https://creativecommons.org/licenses/by-nc-sa/4.0/>).

et al., 2003; Lad et al., 2015; Yu et al., 2020). However, whether the cells are microglia derived is incompletely known in the human context. Moreover, while neuroinflammation is generally thought to contribute to the disease process, the profile and function of these ectopic subretinal immune cells are largely unknown. Here, we set out to elucidate the core phenotypic and functional signature of microglia in degeneration with a focus on the subretinal space, the mechanisms underlying their contributions to disease, and the potential of targeting these cells pharmacologically.

Results

Identification of a common transcriptional signature of subretinal microglia

To investigate the responses by microglia in outer retinal degeneration, we performed single-cell RNA-sequencing (scRNA-seq) of CD45⁺ cells purified from mouse retinas in four distinct model settings. These included (i) 2-month-old wild-type (WT) mice (naïve) as a young adult baseline; (ii) *Rho*^{P23H/+} (P23H) knock-in mice as a genetic model of photoreceptor degeneration (Sakami et al., 2011); (iii) sodium iodate (NaIO₃) model of acute injury to the RPE (Sorsby, 1941); and (iv) 2-year-old WT mice to mimic advanced aging (Fig. 1, A and B; and Fig. S1, A and B). Analysis of these settings identified eight clusters of major immune cell populations, including microglia, monocyte-derived macrophages, perivascular macrophages, monocytes, T cells, B cells, natural killer cells, and neutrophils (Fig. S1 C).

Next, to profile these retinal microglial clusters, we integrated our published dataset of Cx3cr1⁺ sorted retinal cells from mice subjected to light damage (LD; O’Koren et al., 2019), an acute model of photo-oxidative stress-induced photoreceptor degeneration. Successful integration of this dataset was established by the presence of overlapping clusters of microglia, perivascular macrophages, monocyte-derived macrophages, as well as contaminant retinal neurons, but not other immune cells (Fig. 1 A). Integrated analysis of over 15,000 macrophages including microglia revealed comparable cluster types among the four degeneration settings (Fig. 1 B). We had previously identified a cluster that represented microglia that had migrated from their normal positions in the synaptic layers to the subretinal space in the LD model (O’Koren et al., 2019). In the current study, we were able to identify this cluster in all four degeneration models, which was not present in naïve retinas (Fig. 1 C). Differential gene analysis revealed the core transcriptional signature of this microglia cluster that was common among four degeneration models (Fig. 1 D). The top shared upregulated genes included *Lgals3*, *Cd68*, *Gpnmb*, *Fabp5*, *Vim*, *Cstb*, and *Cd63*, while downregulated genes included homeostatic microglial markers, such as *P2ry12*, *Tmem119*, and *Cx3cr1* (Table S1).

As our integrated scRNA-seq analysis revealed that *Lgals3* expression was highly enriched in the microglia cluster of interest (Fig. S1 D), we took advantage of this gene product as a marker for immunolabeling this cluster and examined the co-expression of galectin-3 (Gal3) protein *in situ* and Iba1 in the four distinct models and compared it with naïve mice (Fig. 1 E). As expected, naïve mice do not have subretinal Iba1⁺ cells, and the

microglia in the parenchyma do not express Gal3. In contrast, we observed Gal3⁺ Iba1⁺ cells in all four models predominantly located in the subretinal space, attached to the apical aspect of the RPE. Few to none of the Gal3⁺ Iba1⁺ cells were detected in the plexiform layers of neuroretina (Fig. 1, E and F), suggesting that induction of *Lgals3* upregulation occurs in the subretinal space. Together, our findings suggest the presence of Gal3⁺ subretinal microglia with a common transcriptional signature in distinct forms of retinal degeneration and advanced aged mice. We noted that the morphology of subretinal Iba1⁺ is different among models (Fig. S1, E and F), which is likely due to the distinct features and disease progressions in the individual models.

Deletion of Gal3 in subretinal microglia exacerbates retinal degeneration

Previously, we showed that depletion of endogenous microglia led to excessive accumulation of photoreceptor debris and massive structural damage to the RPE (O’Koren et al., 2019). Here, we investigated whether Gal3 mediates this disease-restricting microglial response in retinal degeneration. We began by analyzing global *Lgals3* knockout (KO) mice and confirmed that young adult naïve *Lgals3* KO mice at the age of 2 months had normal RPE morphology and marginal subretinal Iba1⁺ cells (Fig. 2, A and B; and Fig. S2 A), consistent with a previous report (Esposito et al., 2021). Next, we subjected young *Lgals3* KO and age-matched WT mice to the LD model and compared their retinal phenotypes. *Lgals3* KO mice had substantially increased dysmorphic RPE and elevated TUNEL⁺ cells in photoreceptor layers compared with WT (Fig. 2, A–D), phenocopying the microglia depletion setting in LD shown in a prior study (O’Koren et al., 2019). To assess if Gal3 has an impact on phagocytosis by subretinal microglia, we examined the rhodopsin level in the subretinal Iba1⁺ cells. The results showed that *Lgals3* KO mice failed to engulf dead photoreceptors (Fig. 2 E) and showed a dramatic drop of rhodopsin⁺ subretinal microglia and a massive accumulation of photoreceptor debris (Fig. 2 E), implicating a critical role of Gal3 in the clearance of dead photoreceptors. The augmented damage could not have been due to subretinal Iba1⁺ cell quantity as their densities were comparable in both groups (Fig. S2, A and B). Next, we compared these mice in the advanced aging setting at the age of 2 years. Aged *Lgals3* KO mice showed increased RPE size and reduced visual function measured by electroretinograms (ERG) with attenuated scotopic a-waves and b-waves (Fig. 2, G–I). Finally, we bred *Lgals3* KO onto P23H mice, a clinically relevant mouse model of retinitis pigmentosa (Sakami et al., 2011). Despite comparable subretinal Iba1⁺ cell numbers (Fig. S2, C and D), loss of Gal3 led to electrophysiological deficits (Fig. 2 J and Fig. S2 E) and augmented thinning of photoreceptor layers (Fig. 2 K and Fig. S2 F) in P23H mice. Similar phenotypes of *Lgals3* KO mice were also recently reported in NaIO₃ model (Lew et al., 2022). Collectively, these data demonstrate that Gal3 plays a protective role in different forms of retinal degeneration.

We next wanted to determine the microglia-specific role of Gal3 *in vivo*, as this protein can also be expressed by monocyte-derived cells, Müller cells, and astrocytes. We bred *Lgals3*^{fl/fl} mice (Maupin et al., 2018) onto a C57BL/6J background and then

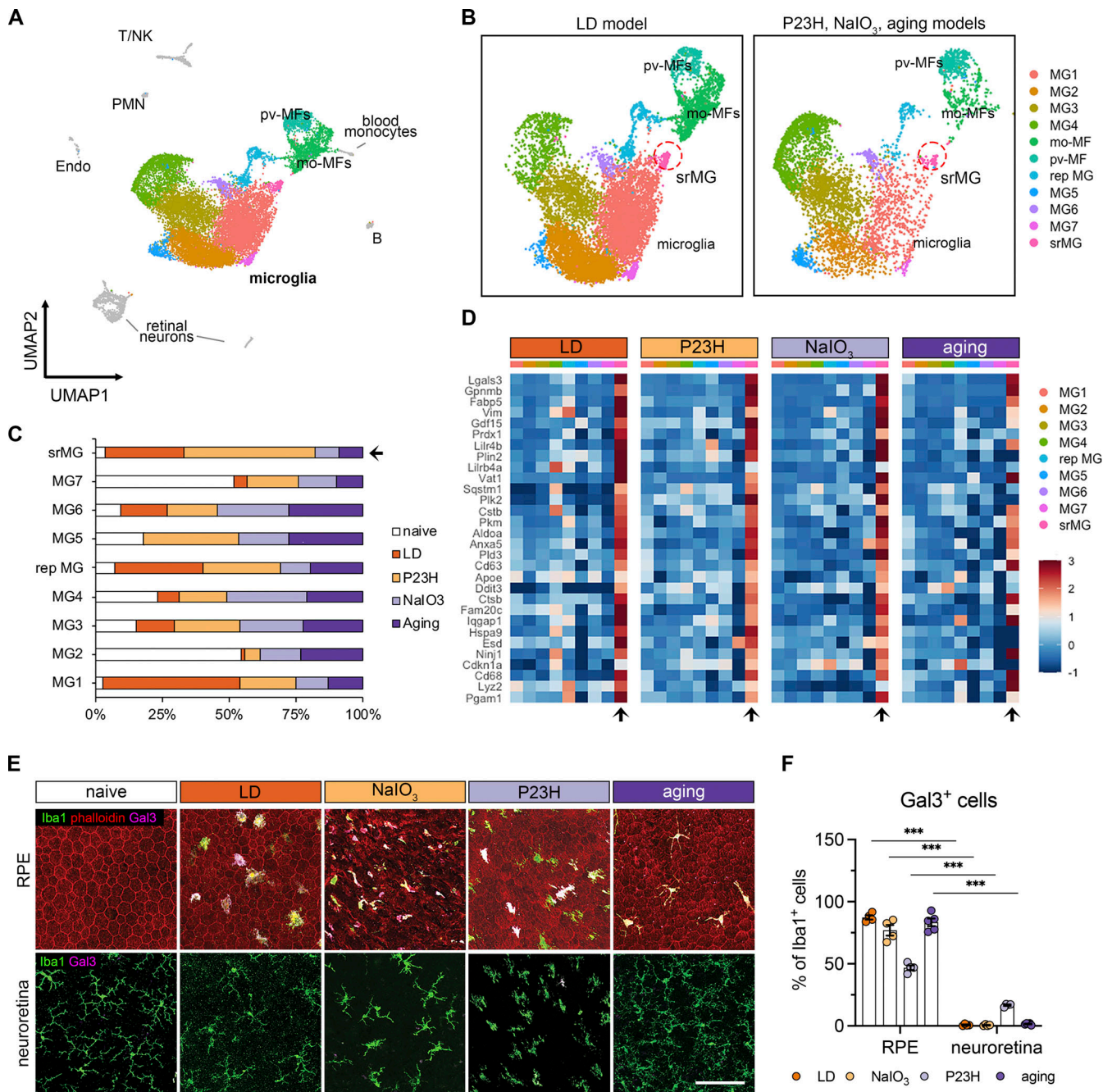


Figure 1. The microglial population present in the subretinal space shares a common signature in mouse models of photoreceptor degeneration, RPE degeneration, and advanced aging. (A) UMAP plot showing integrated clustering of immune cells sampled from four mouse models of retinal degeneration, including LD model (sorted by *Cx3cr1*⁺), NaIO₃ model (CD45⁺), P23H model (CD45⁺), and aging model (CD45⁺) and naïve mice (CD45⁺). A total of 15,623 macrophages, including 13,489 microglia, were integrated among four mouse models. PMN, polymorphonuclear neutrophils; mo-MFs, monocyte-derived macrophages; pv-MFs: perivascular macrophages; NK, natural killer. (B) UMAP plots showing integrated macrophage clusters by two datasets. Dash circles indicate subretinal microglia (srMG). (C) Percentage of sample distribution by clusters. The arrow indicates the enrichment of srMG cluster from degenerating retinas. (D) Heatmap of top 30 conserved marker genes of subretinal microglia shared by each model across clusters. Genes were ranked by fold changes. Arrows indicate srMG cluster. (E) *In situ* validation of Gal3 expression on the apical RPE (top) or in the neuroretina from the inner plexiform layer (bottom). Iba1 (green), phalloidin (red, only in RPE), and Gal3 (magenta). Scale bar: 100 μ m. (F) Percentage of Gal3⁺ cells relative to Iba1⁺ cells between RPE and neuroretina tissues across models. Data were collected from two independent experiments for sequencing and validation. ***: P < 0.001. Two-way ANOVA with Tukey's post hoc test (F).

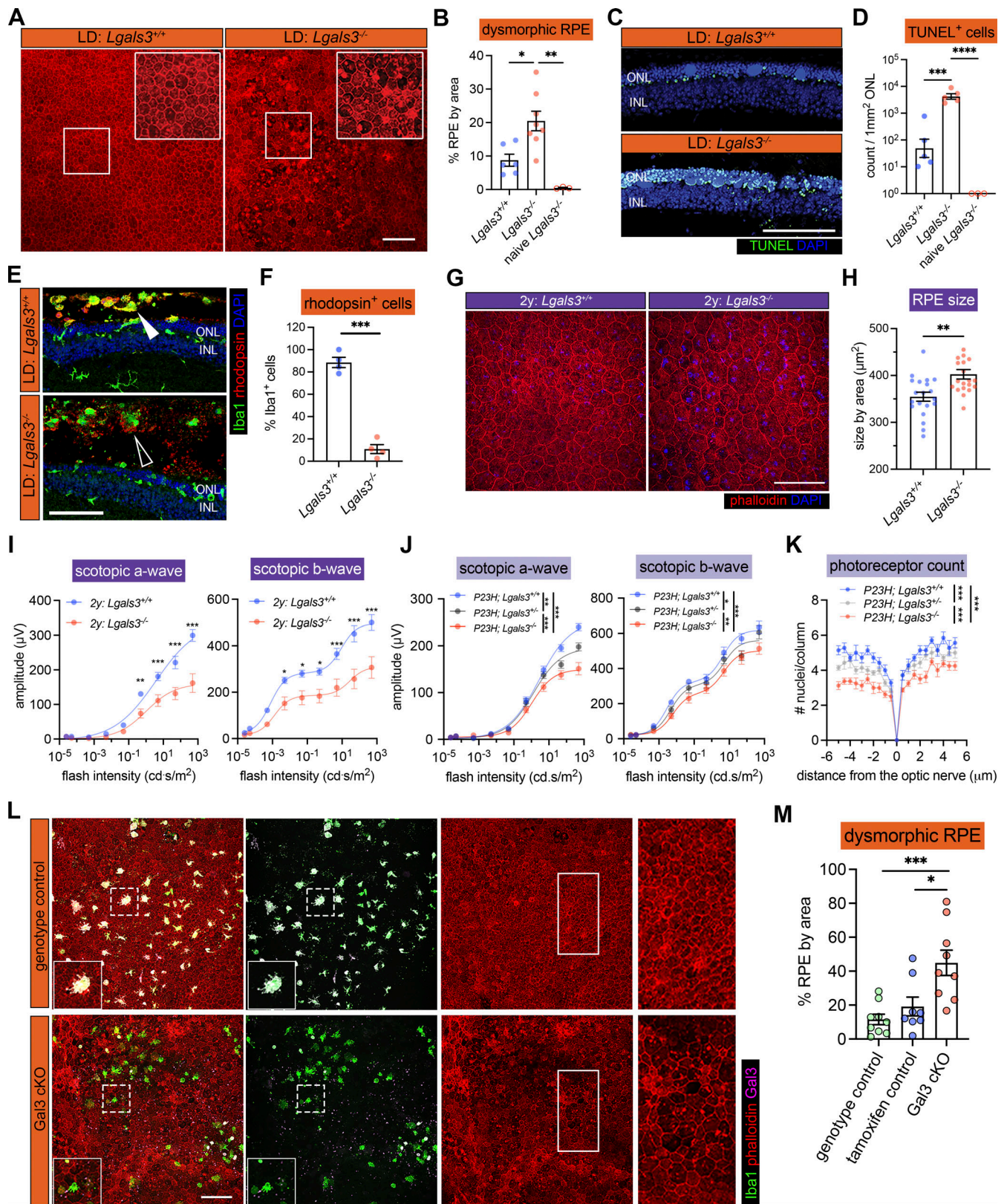


Figure 2. Gal3 expressed by subretinal microglia is central in restricting disease progression in acute, genetic, and aging mouse models of retinal degeneration. (A) Images of phalloidin staining in WT and *Lgals3*^{-/-} RPE tissues in LD. (B) Quantifications of dysmorphic RPE cells (n = 6, 7, and 3, respectively). (C) TUNEL (green) and DAPI (blue) staining in WT and *Lgals3*^{-/-} retinal cross-sections in LD. INL, inner nuclear layer. (D) Quantifications of TUNEL⁺ photoreceptors in ONL (n = 5, 5, and 3, respectively). (E) Rhodopsin (red) and Iba1 (green) staining in WT and *Lgals3*^{-/-} retinal cross-sections in LD. Images from single planes of confocal scans were shown. (F) Quantifications of rhodopsin⁺ subretinal microglia (n = 4 per group). (G) Images of phalloidin staining in WT and

Lgals3^{-/-} RPE tissues at 2 years (2y) of age. **(H)** Quantifications of RPE cell size. Dots represent individual images with $n = 5$ mice per group. **(I)** ERG data showing scotopic a- and b-waves in 2-year-old WT ($n = 5$) and *Lgals3*^{-/-} ($n = 5$) mice. **(J)** Scotopic a- and b-waves of ERG data among *Lgals3*^{+/+} ($n = 12$), *Lgals3*^{+/-} ($n = 6$), and *Lgals3*^{-/-} ($n = 10$) in P23H mice. **(K)** Quantifications of ONL thickness among *Lgals3*^{+/+} ($n = 7$), *Lgals3*^{+/-} ($n = 7$), and *Lgals3*^{-/-} ($n = 8$) in P23H mice. **(L)** Representative images of dysmorphic RPE cells in Gal3 cKO in LD. Iba1, green; phalloidin, red; Gal3, magenta. **(M)** Quantifications of dysmorphic RPE cells in Gal3 cKO mice ($n = 9$) compared with genotype control (*Cx3cr1*^{CreER/+}*Lgals3*^{fl/fl} mice, $n = 9$) and tamoxifen control (*Cx3cr1*^{CreER/+} mice treated with tamoxifen, $n = 8$). Scale bars: 100 μm . Data were collected from two to three independent experiments. *: $P < 0.05$; **: $P < 0.01$; ***: $P < 0.001$; ****: $P < 0.0001$. One-way ANOVA with Tukey's post hoc test (B, D, and M); unpaired Student's t test (F and H); two-way ANOVA with Tukey's post hoc test (I, J, and K).

crossed these mice with *Cx3cr1*^{CreER} for a microglial conditional KO (cKO). We included the genotype control (*Cx3cr1*^{CreER/+}; *Lgals3*^{fl/fl} without tamoxifen) and tamoxifen control (*Cx3cr1*^{CreER/+} with tamoxifen) groups. Considering the critical role of *Cx3cr1* in regulating microglial function and sensitivity to light-induced retinal degeneration (Combadière et al., 2007; Ye et al., 2020), we only used *Cx3cr1*^{YFP-CreER} heterozygous mice hereafter and tested subjecting these mice to the LD model. With these Gal3 cKO mice, we achieved ~75% deletion efficiency of Gal3 in subretinal microglia (Fig. 2 L and Fig. S2 G), but no change was observed in the densities of subretinal Iba1⁺ cells (Fig. S2 H). Our results showed that Gal3 cKO mice had increased TUNEL⁺ photoreceptors (Fig. S2, I and J). Moreover, Gal3 cKO mice also showed decreased rhodopsin⁺ subretinal microglia and increased accumulation of photoreceptor debris (Fig. S2, I and J). Lastly, we observed that Gal3 cKO mice had increased dysmorphic RPE cells (Fig. 2 M). All of these features were consistent with the findings of global *Lgals3* KO mice. Collectively, these results demonstrate that Gal3 contributes to the protection by subretinal microglia but is not required for microglial migration.

Trigger receptor expressed on myeloid cell 2 (Trem2) regulates microglial subretinal migration and Gal3 expression

Our integrated scRNA-seq analysis revealed the upregulation of genes associated with Trem2 signaling in subretinal microglia, including *Syk*, *ApoE*, and *Ctnnb1* (Fig. 3 A). We also found that protein levels of Trem2 and its downstream effector tyrosine kinase Syk were dramatically increased in subretinal microglia (Fig. 3, B and C), although *Trem2* mRNA level remained relatively unchanged in scRNA-seq (Fig. 3 A). Based on a recent study showing Gal3 as a novel ligand of Trem2 (Boza-Serrano et al., 2019), we tested the hypothesis that Trem2 regulates Gal3-mediated function by subretinal microglia. Following this lead, we coimmunolabeled Iba1, Trem2, and Gal3 on the retinas from LD-subjected mice, where we previously demonstrated the predominance of microglia in subretinal space (O'Koren et al., 2019). Our results revealed the colocalization of Trem2 and Gal3 in subretinal microglia (Fig. 3 D). Specifically, Trem2 and Gal3 were colocalized on the surface side of subretinal microglia facing the apical aspect of RPE (Fig. 3 D and Fig. S3 A). Hence, our results implicate a functional specification of Trem2-Gal3 interactions by subretinal microglia in restricting RPE injury and other aspects of retinal degeneration.

To examine whether Trem2 mediates the protective microglia response, we pharmacologically inhibited Trem2 signaling using anti-Trem2 mAb178 via tail vein injection in mice before LD exposure. This antibody blocks the ligand binding of lipidated high-density lipoprotein and Trem2 signaling (Molgora et al., 2020; Turnbull et al., 2006). Our results showed that

Trem2 blockade led to increased subretinal white lesions (Fig. S3 B). However, unlike *Lgals3* deletion, Trem2 blockade led to a reduction of subretinal Iba1⁺ cells (Fig. S3, C and D), suggesting that Trem2 mediates migration of microglia to the subretinal space (Mazaheri et al., 2017; Wang et al., 2015; Zheng et al., 2017). The observed reduction was accompanied by reduced Gal3 expressing Iba1⁺ cells in the subretinal space and amplified RPE dysmorphogenesis (Fig. S3, E-G), therefore suggesting a link between Gal3 and Trem2 activity with microglial-mediated neuroprotection.

We next examined if this Trem2-mediated response is microglia-specific by crossing *Cx3cr1*^{CreER} with *Trem2*^{fl/fl} mice to achieve microglial Trem2 cKO. With an 85% Trem2 deletion efficiency in retinal microglia (Fig. 3, E and F; and Fig. S3, H and I), LD-subjected Trem2 cKO mice had reduced subretinal Iba1⁺ cells and Gal3 expression (Fig. 3, G and H; and Fig. S3 J). Subretinal microglia in these Trem2 cKO mice also appeared morphologically less distended (Fig. 3 E), which is consistent with reduced phagocytic activity (Hsieh et al., 2009; Parhizkar et al., 2019; Wang et al., 2015). Corroborating results with pharmacologic Trem2 blockade, we observed enhanced subretinal white lesions via funduscopy (Fig. 3 I) and increased RPE damage (Fig. 3, J and K) in Trem2 cKO relative to controls in the LD model. These findings suggest that Trem2 is critical in microglial-mediated protection by regulating subretinal migration and is associated with inducing Gal3 expression.

Augmentation of Trem2 activity ameliorates retinal degeneration in a Gal3-dependent manner

Elevated levels of soluble TREM2 were observed in the cerebrospinal fluid of Alzheimer's patients (Ewers et al., 2019; Morenas-Rodríguez et al., 2022). To determine whether increased levels of soluble Trem2 are also found in response to retinal degeneration, we measured soluble Trem2 in vitreous and retinal fluids collected from LD-subjected mice versus naïve controls. We found substantially increased soluble Trem2 levels in LD fluid samples compared with those collected from naïve controls (Fig. 4 A). In contrast, Trem2 cKO mice subjected to LD had a reduced level of soluble Trem2, indicating a microglia-derived origin (Fig. 4 A). Therefore, these findings support our observations on increased Trem2 expression and previous reports of elevated α -secretases, including ADAM10/17 in retinal degeneration as well (Ma et al., 2021; Park et al., 2015).

To test the hypothesis that a Trem2 gain-of-function would further promote its activity and thereby lead to additive protection, we leveraged a recently developed dual-functional 4D9 anti-Trem2 antibody. This antibody binds the Trem2 stalk region recognized by ADAM10/17 to impede ectodomain shedding, and cross-link and stabilize Trem2 expression on the

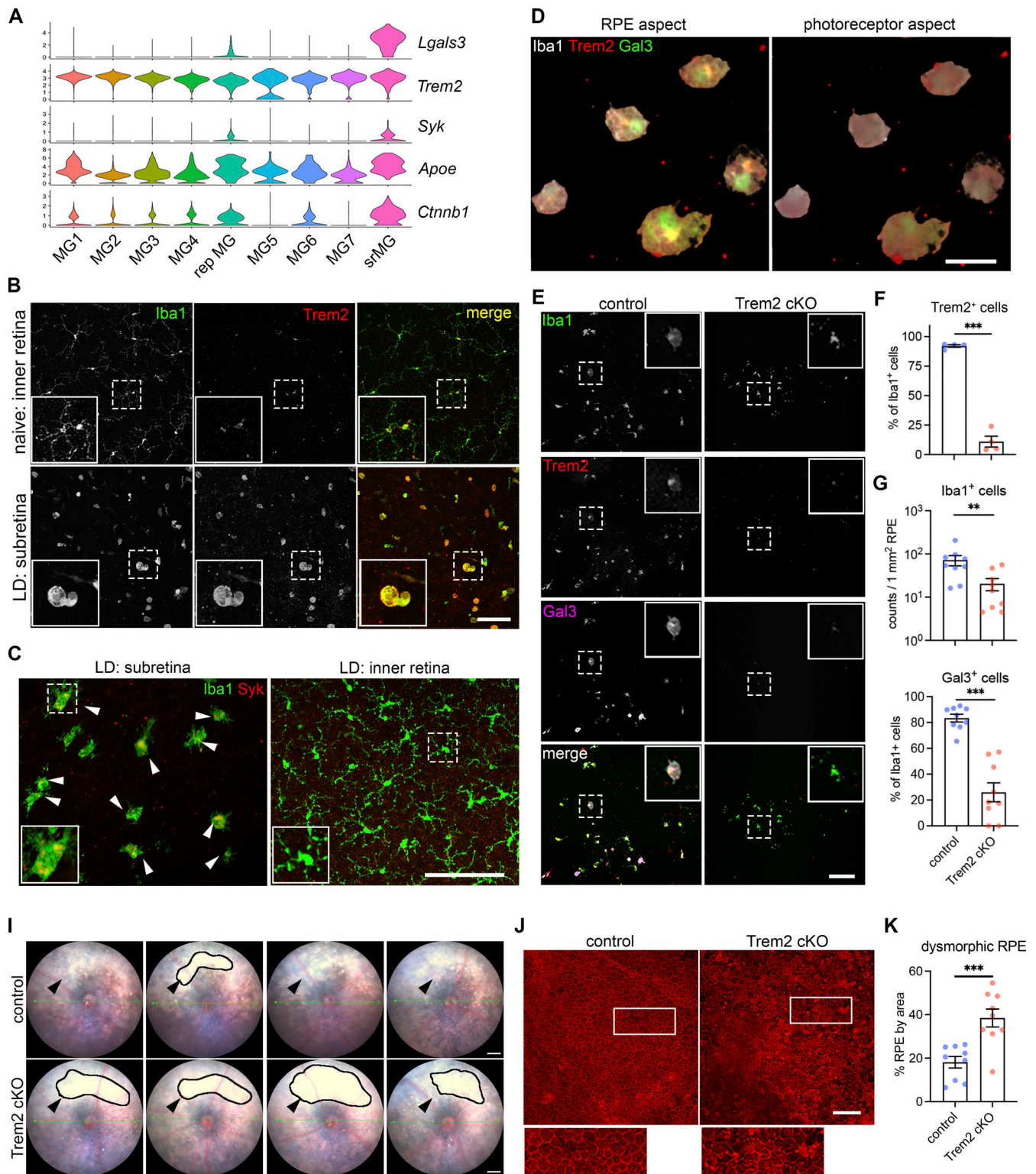


Figure 3. Trem2 regulates microglial migration and promotes Gal3-mediated protection. (A) Violin plots showing the upregulation of genes (*Lgals3*, *Syk*, and *Ctnnb1*) related to Trem2 signaling by subretinal microglia from the integrated dataset of all four mouse models. (B) Images of Iba1 (green) and Trem2 (red) staining in naïve microglia from the inner retina and subretinal microglia in LD. (C) Images of Iba1 (green) and Syk (red) staining in subretinal microglia and microglia from the inner retina in LD. Arrowheads indicate Syk⁺ microglia. (D) 3D rendering images of Gal3 (green), Trem2 (red), and Iba1 (white) staining in subretinal microglia in LD. Views from both the apical RPE aspect and the neuroretina aspect are shown. (E) Images of Iba1 (green), Trem2 (red), and Gal3 (magenta) staining in subretinal microglia between control and Trem2 cKO mice in LD. (F–H) Quantifications of Trem2 depletion (F, *n* = 4 per group), Iba1⁺ cells (G, *n* = 9), and Gal3⁺ cells (H, *n* = 9) between control and Trem2 cKO mice. (I) Fundus images showing increased subretinal white lesions in Trem2 cKO mice in LD as indicated by arrowheads. Images from four individual mice per group are shown. (J) Images of phalloidin staining in RPE tissues from control and Trem2 cKO mice in LD. (K) Quantifications of dysmorphic RPE cells between control and Trem2 cKO mice (*n* = 9 per group). Scale bars: 50 μm (D); 100 μm (B, C, E, and J); 0.5 mm (I). Data were collected from two independent experiments. **: *P* < 0.01; ***: *P* < 0.001. Unpaired Student's *t* test (F–H).

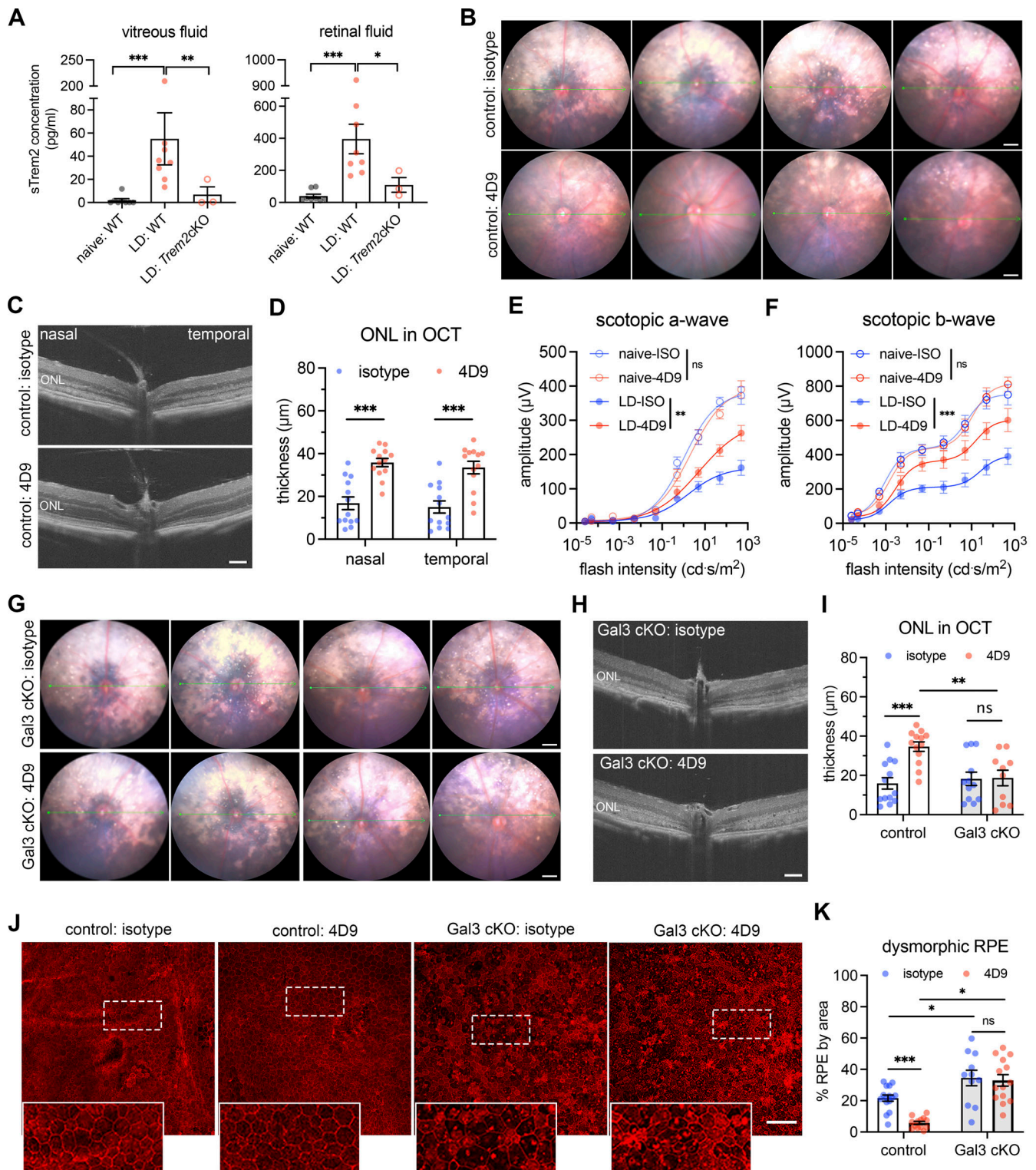


Figure 4. **Bolstering Gal3-dependent Trem2 signaling by microglia prevents retinal degeneration.** (A) ELISA of soluble Trem2 (sTrem2) in vitreous fluid and retinal fluid from naive WT mice, WT, and Trem2 cKO mice subjected to LD. (B) Fundus images of mice treated with isotype control or 4D9 anti-Trem2 in LD. Four individual mice per group are shown. (C) Representative OCT images of mice treated with isotype or 4D9 in LD. (D) Quantifications of ONL thickness by OCT ($n = 13$ per group). ONL thickness was measured at both nasal and temporal sides. (E and F) Scotopic a-waves and b-waves of ERG data among mice treated with isotype or 4D9 in naive or LD setting ($n = 5$ per group). (G) Fundus images of Gal3 cKO mice treated with isotype or 4D9 in LD. Four individual mice per group are shown. (H) Representative OCT images of Gal3 cKO mice treated with isotype control or 4D9 anti-Trem2 in LD. (I) Quantifications of average ONL thickness by OCT between control and Gal3 cKO mice treated with either isotype or 4D9 ($n = 13$ per group). (J) Images of phalloidin staining of control and Gal3 cKO RPE treated with isotype or 4D9 in LD. (K) Quantifications of dysmorphic RPE cells ($n = 15, 13, 11,$ and $13,$ respectively). Scale bars: 0.5 mm (B and G); 100 μm (C, H, and J). Data were collected from two to four independent experiments. *: $P < 0.05$; **: $P < 0.01$; ***: $P < 0.001$; ns: not significant. Unpaired Student's t test (F–H). One-way ANOVA with Tukey's post hoc test (A); two-way ANOVA with Tukey's post hoc test (D–F, I, and K).

microglial surface, thereby promoting phospho-Syk signaling (Schlepckow et al., 2020). Specifically, we examined whether 4D9 can ameliorate degeneration outcomes in the LD model. We administered one dose of 4D9 or isotype antibody to mice via tail vein injection before LD exposure. Fundoscopy showed that retinal injury was substantially reduced in 4D9-treated mice compared with isotype controls (Fig. 4 B). Likewise, optical coherence tomography (OCT) images revealed preservation of the photoreceptor layer with over twofold increase on average in 4D9-treated mice (Fig. 4, C and D). Consistent with the OCT changes, scotopic ERGs showed that 4D9 treatment protected visual function compared with isotype controls in degeneration (Fig. 4, E and F). In addition, the human IgG domain of 4D9 antibodies was predominantly detected in subretinal microglia but was rarely observed in Iba1⁺ cells within the inner retina (Fig. S4, A–C), implicating the added protection was derived from subretinal microglia. Therefore, we show that pharmacologic augmentation of Trem2 activity in subretinal microglia protects the retina from degeneration.

Lastly, we sought to address whether Trem2 and Gal3 are functionally interdependent in microglial-mediated neuroprotection by testing whether 4D9 ameliorates retinal degeneration in Gal3 cKO mice. Analyses using fundoscopy and OCT imaging showed the protection rendered via 4D9 treatment was lost in Gal3 cKO mice, as white subretinal lesions and photoreceptor thickness were indistinguishable between 4D9 and isotype (Fig. 4, G–I; and Fig. S4 D). We also evaluated the impact of 4D9 treatment on the preservation of RPE integrity. Our results showed that 4D9 treatment better preserved RPE morphology relative to isotype in control mice, whereas this protective effect was lost in Gal3 cKO mice (Fig. 4, J and K). However, the frequencies of subretinal microglia did not significantly change between isotype and 4D9 treatments (Fig. S4 E). Together, our findings show that added protection by Trem2 agonist is associated with Gal3 expressed by subretinal microglia, thereby further supporting their functional interdependence.

Microglia at the sites of atrophy show a conserved molecular phenotype and are enriched in the macula of AMD patients

To address the significance of our findings in the human context, we performed another scRNA-seq of myeloid cells from post-mortem neuroretina and RPE/choroid tissues of eight human donors at the age of over 70, including three AMD cases (Table S2). For each donor, we used one eye to evaluate the retinal and choroidal pathology (Lad et al., 2015), and we sorted CD45⁺CD11B⁺ cells using the contralateral eye. We captured 14,873 myeloid cells that passed quality control, making it a valuable resource to uncover microglial states in human retinal tissues. Similar to mouse models studied in our aforementioned experiments, our unsupervised clustering results of neuroretina and RPE/choroid tissues revealed five clusters of three major macrophage cell types, including microglia, perivascular, and monocyte-derived macrophages (Fig. 5 A, Fig. S5 A, and Table S3). Among these clusters, human retinal microglia specifically expressed *TMEM119*, *TREM2*, and *CX3CR1*, while perivascular and monocyte-derived macrophages can be distinguished by the expression of *LYVE1* and *CCR2*, respectively (Fig. 5 B).

To determine which human macrophage cluster represents subretinal microglia in AMD, we utilized the identified mouse marker genes of subretinal microglia, homeostatic microglia, and other macrophages from mice (O’Koren et al., 2019), and calculated the corresponding human gene module scores of these macrophage clusters (Tirosh et al., 2016). Two of the human macrophage clusters gained the highest scores of perivascular and monocyte-derived macrophages, respectively, corroborating the identities determined above (Fig. 5 C). By contrast, the hMG2 cluster showed the highest similarity to subretinal microglia (Fig. 5 C). Interestingly, the hMG2 cluster is also composed of more cells from RPE/choroid tissues compared with the other two microglia clusters (Fig. 5 D and Fig. S5 B), which is consistent with the knowledge that subretinal microglia adhere to the apical RPE, and thereby leading us to hypothesize that hMG2 cluster represents subretinal microglia in human AMD. To examine the similarities between mouse subretinal microglia and the hMG2 cluster, we directly compared their gene expression profiles. Among 1,341 differentially expressed genes (DEGs) shared by mice and humans, 87.99% of these genes are similarly changed, including 1,159 upregulated genes and 21 downregulated genes (Fig. 5 E). The pathway enrichment analysis of top shared upregulated genes inferred functions in phagocytosis, responses to oxidative stress, and lipid metabolism (Fig. S5 C), which is in line with our mouse findings. Also, *LGALS3* is enriched in cells of hMG2 clusters from AMD patients and *CD68* is expressed by all microglia clusters (Fig. 5 F). Hence, transcriptomic analysis suggests a conserved profile for subretinal microglia between mice and humans.

To investigate whether the hMG2 cluster is significantly associated with human AMD, we extracted myeloid cells by *AIF1* expression from another two publicly available datasets of independent AMD studies and integrated them with our dataset. The integrated dataset contains 39,754 myeloid cells collected from a total of 39 human donors with 20 AMD patients and 19 age-matched controls (Fig. 5 G). Our integrated analysis revealed similar clusters among three datasets (Fig. S5, D–F), with the exception of a *RHO*^{high} microglia cluster exclusively derived from one AMD donor with neovascularization (Fig. S5 G). The GSE183320 dataset, which does not contain cells from neuroretina, showed a substantial decrease of microglial cells compared with the other two datasets, especially for hMG1 and hMG3, supporting a proper data integration (Fig. 5 G and Fig. S5 F).

To determine which cells belong to the hMG2 cluster in the integrated datasets, we used two independent approaches. One approach was via labeling transfer by Seurat package (Fig. 5 H); the second was via subclustering to determine *LGALS3* expressing clusters (Fig. S5, H and I). Both approaches showed similar results for the hMG2 frequencies. Specifically, we found that frequencies of hMG2 significantly increase in the macula of RPE/choroid tissues from AMD donors (Fig. 5 I and Fig. S5 J). The hMG2 cluster was also present in the elderly non-AMD group but with a lower frequency (Fig. 5 J and Fig. S5 K), which may represent a part of normal aging as seen in our mouse aging model. Taken together, we conclude that these subretinal microglia are most enriched in the locations associated with tissue atrophy of human AMD.

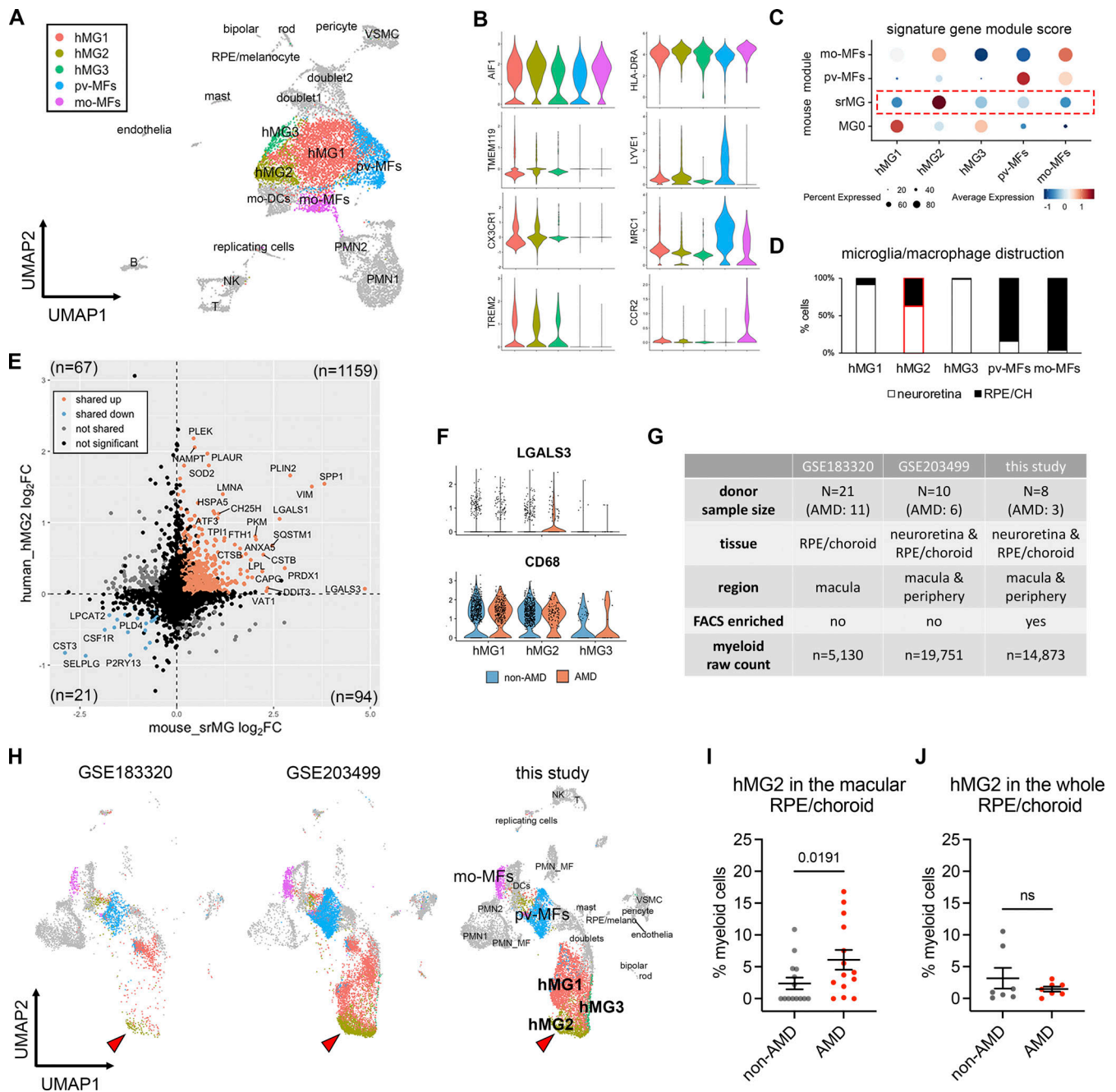


Figure 5. Microglia at the sites of atrophy show a conserved phenotype between mice and humans and are enriched in the macula of AMD patients. (A) UMAP plot showing unsupervised clustering analysis of myeloid cells from human donors. CD45⁺CD11b⁺ cells were FACS-sorted from neuroretina and RPE/choroid tissues, respectively. hMG, human microglia; mo-MFs, monocyte-derived macrophages; pv-MFs: perivascular macrophages; mo-DCs, monocyte-derived dendritic cells; VSMC, vascular smooth muscle cells. (B) Violin plots showing the marker expression by macrophage clusters. (C) Dot plots showing gene module scores of human microglia/macrophage clusters. The gene modules were generated and normalized using the top 200 mouse markers from homeostatic microglia (MG0), subretinal microglia (srMG), pv-MFs, and mo-MFs. (D) Bar graphs showing the composition of macrophage/microglia clusters by tissues. The red box indicates the enrichment of cells from RPE/choroids in hMG2 cluster. (E) Comparison of gene expression between mouse subretinal microglia (x-axis) and human hMG2 (y-axis). The number in each quadrant shows the quantity of DEGs as indicated by colors. (F) Violin plots showing the expression of *LGALS3* and *CD68* by microglia clusters between non-AMD and AMD donors. (G) Summary of three independent human AMD scRNA-seq datasets. (H) UMAP plots showing the label transfer of myeloid cells among datasets. Arrowheads indicate hMG2 clusters in each dataset. (I and J) Quantifications of hMG2 frequencies in the whole and macular RPE/choroid tissues between non-AMD and AMD donors. Mann-Whitney test (one-tailed) was used, and P values are shown; ns: not significant.

In situ evidence and correlation of subretinal microglia expressing GAL3 and TREM2 in AMD subjects

Lastly, we validated the presence of these subretinal microglia in AMD by immunohistochemically staining human postmortem tissues from another cohort of $n = 18$ aged non-AMD and AMD donors (Table S2) using antibodies against human GAL3 and CD68, two markers of the subretinal microglia population that were previously validated in mice (O'Koren et al., 2019). Immunolabeling was performed on tissues sectioned through the macular region and classified according to the Sarks AMD grading scale of disease severity (Lad et al., 2015). Multispectral imaging revealed GAL3⁺CD68⁺ cells, stained orange-red due to coexpression, were predominantly observed in the subretinal space but rarely in the inner retina (Fig. 6 A). The GAL3⁺CD68⁺ cells were primarily located between the neurosensory retina and the RPE, adherent to basal deposit in areas of absent RPE, and within the basal deposit between RPE and Bruch's membrane (Fig. S6 A). We found that GAL3⁺CD68⁺ cells were enriched in the subretinal space within the macula in Sarks stages IV to VI (intermediate to advanced AMD), but not in aged controls represented by Sarks stages I (normal) and II (aging) or III (early AMD; Fig. S6 A). The double-positive cells were enriched in the regions of geographic atrophy (GA) with RPE loss (Fig. 6 B and Fig. S6 B) but also present in the areas of photoreceptor loss with preserved RPE cells, including the transitional area of AMD macula (Fig. S6 C). Moreover, we identified a strong positive correlation between Sarks AMD grades and the frequencies of these double-positive cells in the subretinal space of the macular region (Fig. 6 C). These findings corroborate our observed enrichment of the hMG2 cluster in the macular region of human AMD subjects. In addition, we observed that our sections from both age-matched controls and AMD subjects exhibited age-related peripheral retinal degeneration, including peripheral cystoid and ischemic (paving stone) degeneration (O'Malley et al., 1965; O'Malley and Allen, 1967; Wolter and Wilson, 1959), wherein subretinal GAL3⁺CD68⁺ cells were also observed (Fig. S6 D). This may partially explain the presence of hMG2 with low frequencies in aged non-AMD subjects. Of note, the frequencies of subretinal cells may be underestimated because we analyzed retinal cross-sections within the macula but not the whole macula. Taken together, these data suggest that the presence of subretinal GAL3⁺ CD68⁺ cells is a response to degeneration of the outer retina and these cells are enriched in GA.

To determine whether TREM2 expression is relevant in human AMD, we analyzed flow cytometry data from the same cohort of human donors used for generating the scRNA-seq in this study (Fig. S6 E and Table S2). We observed that the frequencies of TREM2⁺ myeloid cells (CD45⁺CD11B⁺) were elevated in the RPE/choroid tissues from AMD donors, while the frequencies of CD45⁺ and CD11B⁺ cells remained relatively unchanged (Fig. 6, D–G; and Fig. S6 F). From our scRNA-seq dataset, we can conclude that the identity of TREM2⁺ myeloid cells is likely microglia. Moreover, we found that the frequencies of TREM2⁺ myeloid cells are strongly correlated with AMD progression (Fig. 6 H), further supporting our results for subretinal GAL3⁺CD68⁺ histologically. Of note, we attempted to immunolabel for TREM2 histologically in retinal sections with

anti-human TREM2 antibodies (R&D AF1828 and LSBio LS-B16999), but without success, as others have reported similar technical issues with formalin-fixed and paraffin-embedded CNS tissues (Fahrenhold et al., 2018; Satoh et al., 2013). Therefore, our collective findings using orthogonal approaches implicate the conserved presence of subretinal microglia and involvement of GAL3-TREM2 in human AMD.

Discussion

Our results uncovered a common population of microglia in the subretinal space that restricts disease progression across multiple distinct mouse models of retinal degeneration. Likewise, we identified microglia with a conserved profile at the transcriptomic, protein, and spatial levels that are present and enriched in the macula of human subjects with GA. The accumulation of subretinal macrophages has been documented in many, if not most, retinal degenerative diseases (Combadière et al., 2007; Greferath et al., 2016; Gupta et al., 2003; Kohno et al., 2013; Lad et al., 2015; Tang et al., 2017), and the protective subretinal microglial signature we defined may represent a general response in these disease settings. Although the mouse models used in our study may not represent all clinical aspects of human AMD, our data revealed over 87% of DEGs were shared between mice and humans, and overlapped functional inferences (such as phagocytosis and lipid activity). Hence, our findings may lay the molecular foundation for using mouse models to understand subretinal microglial responses in human retinal degeneration.

Our results revealed that within the microglial compartment, only subretinal microglia upregulate Gal3 expression, though we do acknowledge that Gal3 can be expressed by non-microglial cells, such as infiltrated monocyte-derived macrophages, astrocytes, and retinal Müller glia in the CNS disease settings (Mehina et al., 2021; Sirko et al., 2015; Uehara et al., 2001). Indeed, several studies using *Lgals3* global KO mice have reported that Gal3 acts pathologically in models of neurodegeneration (Boza-Serrano et al., 2019; Siew et al., 2019; Tao et al., 2020) and promotes loss of retinal ganglion cells in glaucoma (Margeta et al., 2022). The crux of our experiments explicitly focused on microglia via the use of *Cx3cr1^{CreER}* mice, which helped identify the isolated roles of Gal3 in microglial-mediated phagocytosis of dead photoreceptors and RPE protection. By contrast, one recent study reported that Gal3 inhibition appears neuroprotective and results in increased retinal thickness in the LD setting (Tabel et al., 2022). However, their increased retinal thickness may be due to deficient phagocytic clearance of dead photoreceptors as identified in our study, and some of the results may be confounded by mouse genetic background. Also, we cannot exclude the possibility that monocyte-derived cells may be present in the outer retina in the AMD (Senlaub et al., 2013) and that subretinal cells may have neuroinflammatory roles (Yu et al., 2020). Hence, further investigation would be needed to understand Gal3-mediated functions in microglial versus non-microglial cells in different neurodegenerative contexts.

Mechanistically, Gal3-mediated protection required upstream Trem2 signaling. The latter, we showed, regulated microglial migration to the subretinal space and induced Gal3

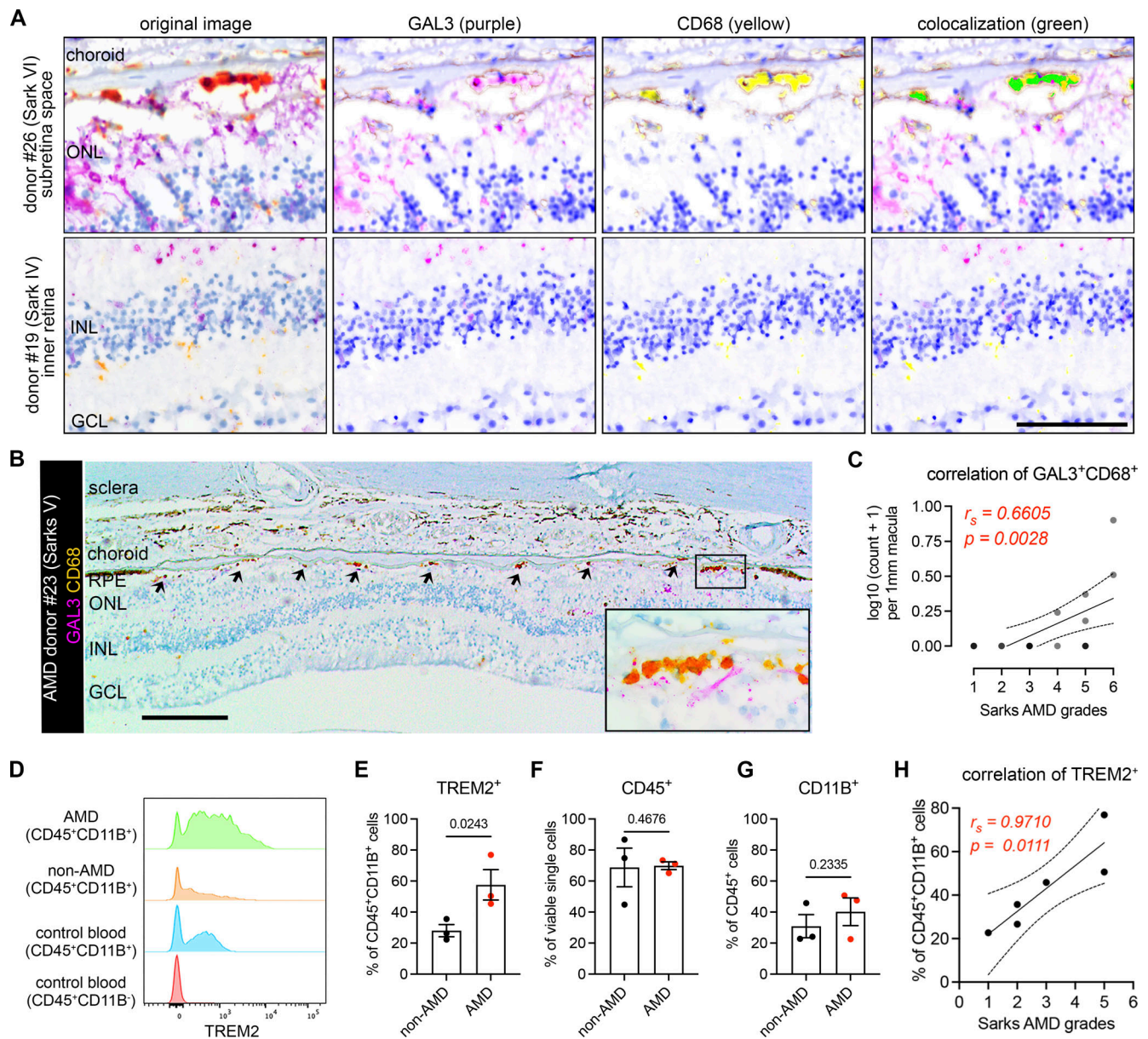


Figure 6. Microglia expressing GAL3 and TREM2 are associated with AMD progression. (A) Multispectral imaging of GAL3 and CD68 co-staining in the subretinal space (top) and inner retina (bottom) from human donors. Unmixed purple spectrum (GAL3) and yellow spectrum (CD68) are shown. The areas of colocalized spectra are highlighted in green. Scale bar: 50 μ m. INL, inner nuclear layer. (B) Representative image of GAL3 and CD68 costaining in the macular GA region of a retinal section from an 88-year-old female donor eye with advanced AMD (Sarks V). Arrows indicate double-positive myeloid cells in GA. The black insert box shows the magnification of GA with double-positive cells. Scale bar: 200 μ m. GCL, ganglion cell layer. (C) Correlation between the frequencies of macular GAL3⁺CD68⁺ double-positive cells (y-axis) and Sarks AMD grading (x-axis) by Spearman's correlation ($n = 18$ donors, Table S2). The coefficient and P value are shown. (D) Histograms showing increased TREM2⁺ myeloid cells (CD45⁺CD11B⁺) in RPE/choroid tissues of AMD donors. Concatenated histograms were shown ($n = 3$ per group). Control human blood samples were used to set up flow gating. (E–G) Quantifications of TREM2⁺ (E), CD45⁺ (F), and CD11B⁺ (G) cell frequencies in RPE/choroid tissues between non-AMD and AMD donors. Unpaired student's *t* test is used. P values are shown. (H) Correlation between the frequencies of TREM2⁺ myeloid cells (y-axis) and Sarks AMD grading (x-axis) in RPE/choroid tissues by Spearman's correlation. The coefficient and P value are shown.

expression. Trem2-mediated signaling may be particularly important for subretinal protection. Indeed, we found upregulated Trem2 protein expression and Syk expression in subretinal microglia. Moreover, 4D9 agonistic antibodies dominantly localize with subretinal microglia, likely due to increased Trem2 expression by these subretinal cells. Our data also corroborate the recent findings on the neuroprotective roles of microglia-

derived Syk in neurodegenerative diseases (Ennerfelt et al., 2022; Wang et al., 2022).

Trem2, a central lipid sensor by microglia (Wang et al., 2015), could mediate neuroprotection via increased phagocytosis, antioxidant activity, and lipid metabolism by subretinal microglia (O'Koren et al., 2019), and facilitate the prompt clearance of dead photoreceptors and cellular debris to support the maintenance

of RPE homeostasis. Congruently, we showed that conditional genetic depletion of microglia (O’Koren et al., 2019) or deletion of Gal3 in this study resulted in the accumulation of dead/dying photoreceptor debris in the subretinal space. Separately, as Trem2-Gal3 colocalization was polarized toward the RPE-facing aspect of subretinal microglia, subretinal microglia may play a direct role in RPE preservation, but these points require further investigation. Interestingly, the transcriptional signature of these subretinal microglia resembles that of disease-associated microglia in neurodegeneration (Keren-Shaul et al., 2017; Krasemann et al., 2017) and is also similar to microglial profiles in development (Anderson et al., 2019; Hammond et al., 2019). Consistent with several studies showing that Gal3 is present in this signature (Krasemann et al., 2017; Lee et al., 2018; Nugent et al., 2020), our study demonstrated that Gal3 is required for Trem2-mediated protection and established their functional association in the retina.

In our study, we also observed elevated levels of soluble Trem2 in retinal degeneration. This elevation in the disease state may result from either increased Trem2 expression by microglia or increased cleavage by secretases (Ma et al., 2021; Park et al., 2015). Indeed, elevated soluble TREM2 was also observed in cerebrospinal fluid from Alzheimer’s patients (Heslegrave et al., 2016; Morenas-Rodríguez et al., 2022; Piccio et al., 2016; Suárez-Calvet et al., 2016a, 2016b), and the strategy to bolster TREM2 activity is being tested in a clinical trial. Hence, our findings that subretinal microglia restrict disease progression via Gal3-Trem2 signaling and that this response can be bolstered pharmacologically may provide a novel focal point for developing potential therapeutic interventions to support photoreceptor and RPE preservation in outer retinal degenerative diseases.

Materials and methods

Mice

All procedures involving animals were approved by the Institutional Animal Care and Use Committee at Duke University, and the procedures were carried out in accordance with the approved guidelines. WT C57BL/6J, *Lgals3*^{-/-} (Stock #006338), *Cx3cr1*^{YFP-CreER} (Stock #021160), and *Trem2*^{fl/fl} mice (Stock #029853) were obtained from the Jackson Laboratory. *Rho*^{P23H} mice (Sakami et al., 2011) were generated as described previously. The frozen sperms of *Lgals3*^{fl/fl} mice (Maupin et al., 2018) were kindly provided by Bart O. Williams from Van Andel Research Institute, Grand Rapids, MI, USA, and were retrieved at Duke University. The rederived mice were further bred into a C57BL/6J background. *Cx3cr1*^{YFP-CreER} mice were crossed with *Lgals3*^{fl/fl} or *Trem2*^{fl/fl} to generate the strains for microglia-specific depletion, respectively. Only heterozygous *Cx3cr1*^{YFP-CreER} mice were used. If not otherwise stated, the mice used included both sexes and were at 8–20 weeks of age. All mice herein did not carry *rd8* mutation and were bred and housed at a barrier-free and specific-pathogen-free facility with a 12-h light/12-h dark cycle at Duke University.

Human autopsy eyes

The metadata of human donors and autopsy eyes are included in Table S2. The use of autopsy eyes for research was approved by

the Institutional Review Board at Duke University. Due to the lack of ophthalmic clinical history in most cases, the diagnosis of AMD was made postmortem. Following the removal of the superior calotte, postmortem fundus examination, and color photography, the eyes were embedded in paraffin and sectioned at 5- μ m thickness. Hematoxylin and eosin, periodic-acid Schiff, and immunostained macular sections were evaluated for the presence of AMD and graded using the AMD grading system by Sarks. Eyes with other detectable macular pathology or with glaucoma were excluded.

LD model

LD in mice was induced, as previously described. Briefly, mice were adapted in darkness overnight, and eyes were dilated with 1% atropine sulfate (Bausch & Lomb) and 10% phenylephrine hydrochloride (Paragon BioTeck). Mice were then placed in a reflective container with a cool white-light LED light source (Fancierstudio), which was placed above the container with 65,000 lux adjusted using an illuminance meter. After 6 h exposure for *Cx3cr1*^{YFP-CreER} mice or 8 h for other C57BL/6J mice, the mice were returned to the housing facility with normal lighting and bred for an additional 5 days before experiments.

Sodium iodate model

2-month-old mice were administered a single dose of sodium iodate (15 mg/kg body weight; Sigma-Aldrich) via intraperitoneal injection. After 5 days, mice were euthanized and retinas were collected for analysis.

Conditional depletion in microglia

Cx3cr1^{YFP-CreER/+}; *Lgals3*^{fl/fl} mice, *Cx3cr1*^{YFP-CreER/+}; *Trem2*^{fl/fl} mice, or *Cx3cr1*^{YFP-CreER/+} control mice were intraperitoneally injected with tamoxifen (75 mg/kg; Sigma-Aldrich) twice, with 1 day in between injections. To target microglia only, after the tamoxifen pulse, mice were rested for 4 weeks before experiments, which spared depletion in monocytes and monocyte-derived cells (O’Koren et al., 2016).

Immunohistochemistry

Mice were euthanized by CO₂ asphyxiation immediately before tissue harvest. Eye tissues were dissected to remove corneas, lenses, irises/ciliary bodies, and optic nerves. Tissues were fixed in 4% paraformaldehyde (PFA) in PBS for 20 min to 1.5 h at room temperature or on ice. Tissues were either sequentially cryoprotected in 15% and 30% sucrose and then embedded in optimal cutting temperature compound (Tissue-Tek) for cryosections or separated into neuroretinas and RPE/choroids for flat mounts. Flat mounts were blocked and permeabilized with 5% FBS in PBS supplemented with 0.5% Triton-X100 and 0.5% Tween-20 and sequentially incubated with primary antibodies and appropriate secondary antibodies. Phalloidin conjugated with Alexa 594 (#A12381; Invitrogen) was included with secondary antibodies to stain F-actin of RPE cells. Primary antibodies used were as follows: rabbit anti-Iba1 (#019-19741; Wako), goat anti-Gal3 (#AF1197; R&D), rat anti-Gal3 (#125401; Biolegend), sheep anti-Trem2 (#AF1729; R&D), mouse anti-rhodopsin (#ab5417; Abcam), and rabbit anti-Syk (#ab40781; Abcam). Images were

acquired using a Nikon A1R confocal laser scanning microscope. A resonant scanner and motorized stage were used to acquire z-stacks. Unless otherwise indicated, maximum projections of image stacks were shown.

Human autopsy eyes were fixed in 3.7% neutral-buffered formaldehyde. The detection of GAL3 and CD68 was performed at Duke Pathology Core facility using The VENTANA DISCOVERY Ultra automated immunohistochemistry staining system (Ventana Medical Systems). Sections were incubated with primary antibodies: rat anti-human GAL3 (#14-5301-82, 1:50 dilution; Invitrogen) and mouse anti-human CD68 (#M0814, 1:400 dilution; Dako), followed by the secondary antibody incubation and chromogenic detection with DISCOVERY Purple and Yellow kits (#760-229 and #760-239; Ventana-Roche Diagnostics). These chromogenic dyes are covalently deposited and have unique spectra (Day et al., 2017) that allow spatial mapping and detection of colocalization using multispectral imaging (Saylor et al., 2018). Cells coexpressing DISCOVERY Yellow and Purple appear orange-red (Jakobiec et al., 2021), and coexpression was confirmed using a Nuance 3.0.2 Multispectral Imaging System (PerkinElmer).

Histology in mice

Euthanized mice were fixed via transcardial perfusion with 2% PFA and 2% glutaraldehyde in 0.1% cacodylate buffer (pH = 7.2). The eye tissues were post-fixed in the same fixative for 24 h and processed in a solution of 2% osmium tetroxide in 0.1% cacodylate buffer, followed by processing with gradient ethanol from 50% to 100%, propylene oxide, and propylene oxide: epoxy 812 compound (1:1 ratio) under the vacuum. Samples were further embedded in fresh epoxy 812 compound resins at 65°C overnight. Semi-thin cross-sections (0.5 μm) across the block were stained with 1% methylene blue.

Morphological analysis of microglia

The covered area and process length of microglia were quantified as previously described (Young and Morrison, 2018). Briefly, images of neuroretina or RPE/choroid flatmounts stained with Iba1 were optimized and transformed into binary ones. The covered area of individual microglia was measured using Analyze Particle in ImageJ, and the average covered area per image was calculated as the total area divided by the number of microglia. To quantify the process length, images were skeletonized and analyzed using the Analyze Skeleton (2D/3D) Plugin in ImageJ. The branch length of individual microglia was summed and divided by the number of microglia. For each mouse model, four mice per group and three images (628.22 \times 628.22 μm) per mouse $n = 4$ mice were analyzed.

Quantifications of RPE dysmorphology and subretinal microglia

RPE dysmorphology was quantified as described previously (O'Koren et al., 2019). RPE flatmounts stained with phalloidin and Iba1 were imaged, and multiplane z-series images were acquired using 20 \times objective (628.22 \times 628.22 μm per image). To avoid the confounding effects from the areas around the optic nerve head and peripheral iris/ciliary bodies, one random image

was acquired in the middle of each RPE quadrant, with a total of four images per RPE flatmount. RPE cells that exhibited either altered lateral or lost apical F-actin morphology were considered dysmorphic. Four complete fields per RPE flatmount were assessed. The numbers of abnormal and total RPE cells were counted in each field, and the mean percentage of RPE dysmorphology in four fields was calculated for each mouse. The frequencies of subretinal microglia per field were determined as total cell counts divided by total areas, and the mean frequency of subretinal microglia in four fields was calculated for each mouse.

TUNEL assay

This assay was performed using *in situ* cell death detection kit (Roche) according to the manufacturer's instructions. Briefly, retinal cross-sections were blocked and stained for TUNEL and DAPI. At least three images of each animal were acquired using Nikon A1R confocal microscopy and analyzed using Image J. The frequencies of TUNEL⁺ cells per 1 mm² in the outer nuclear layer (ONL) were calculated.

Quantifications of phagocytosis by subretinal microglia

Retinal cross-sections were stained with anti-rhodopsin and anti-Iba1 antibodies. Nuclei were counterstained with DAPI. Single planes of confocal scans were used to quantify rhodopsin⁺ microglia in the subretinal space. Three images of each mouse were acquired and the mean percentage of rhodopsin⁺ cells was calculated for each mouse.

OCT and fundus imaging

Mouse eyes were topically dilated with 1% tropicamide and 10% phenylephrine sulfate and anesthetized via intraperitoneal injection with a mixture of ketamine/xylazine. The corneas were kept moist with GenTeal lubricant eye gel (Alcon). Eyes were imaged using Micron IV retinal imaging system (Phoenix Research Labs).

ERG

ERG was measured as previously described (O'Koren et al., 2019). Briefly, the pupils of dark-adapted mice were dilated with 0.5% tropicamide and 1.25% phenylephrine. Mice were then anesthetized with a mixture of ketamine/xylazine. Scotopic and photopic responses were recorded using an Espion E2 system (Diagnosys) with increasing flash intensities (scotopic: from 2.5 $\times 10^{-5}$ to 500 cd.s/m²; photopic: from 5 to 500 cd.s/m² with a background light of 25.5 cd.s/m² intensity). Recordings of single flash presentations were measured 1–15 times to verify the response reliability and improve the signal-to-noise ratio if required.

Treatment of anti-Trem2 antibodies

Cx3cr1^{YFP-CreER/+} mice were injected via tail vein with Fc-mutated mAb178 anti-Trem2 (50 mg/kg) or vehicle control for loss-function, or 4D9 anti-Trem2 (50 mg/kg) or isotype for gain-function, right before dark adaptation of LD.

Quantifications of human IgG containing microglia

To determine the location of 4D9 antibodies, retinal cross-sections and retinal and RPE/choroid flatmounts were stained

with DyLight 594 donkey anti-human IgG, and anti-Iba1 antibodies were imaged with Nikon A1R confocal microscopy. The retinas from mice subjected to LD without 4D9 treatment were used as negative controls for autofluorescence. The human IgG⁺ microglia were counted on the RPE and in the inner retina, and the percentages were shown.

ELISA of vitreous and retinal fluids

Vitreous fluids were collected from euthanized mice using a Hamilton syringe with a 30-gauge needle and immediately mixed with proteinase inhibitors. For retinal fluids, retinas were dissected in a dry dish and then incubated on ice for 10 min with 50 μ l PBS per retina supplemented with proteinase inhibitors. After centrifuging at 14,800 *g* for 5 min, fluid samples were collected. ELISA of soluble Trem2 was measured using DuoSet Ancillary Reagent Kit 2 (R&D) according to the manufacturer's instructions. Recombinant Mouse Trem2 (#1729-T2; R&D) was used to generate a standard curve. Capture antibodies of anti-mouse Trem2 (#AF1729; R&D) and detection antibodies of biotinylated anti-Trem2 (#BAF1729; R&D) were used at 0.4 and 0.1 μ g/ml, respectively. Biotinylated antibodies were detected using streptavidin-HRP (#405210; Biolegend).

scRNA-seq

Mouse retinas were dissected from five males of each model, including 2-month-old naïve WT mice, 2-month-old mice of sodium iodate model, 2-month-old *Rho*^{P23H/+} mice, and 2-year-old WT mice. Retinas of each model were pooled and digested in 1.5 mg/ml collagenase A and 0.4 mg/ml DNase I (Roche) for 45 min at 37°C with agitation. Single-cell suspensions were generated by passing through 70- μ m filters and sequentially stained with APC anti-mouse CD45 (#103111; Biolegend) and propidium iodide (Sigma-Aldrich) for viability. Viable CD45⁺ single cells were collected by fluorescence activated cell sorting (FACS). 10 \times Genomics Single Cell 3' chemistry (v2) was used to generate Gel Bead-In Emulsions (GEM) and perform post GEM-reverse transcription cleanup, cDNA amplification, as well as library construction.

Eye tissues from human donors were recovered within 8 h of death and then dissected to separate neuroretinas and RPE/choroids. Neuroretinas were then homogenized using douncers and RPE/choroids were digested with collagenases A and DNase I for 1 h at 37°C with agitation, respectively. Single-cell suspensions were generated by passing through 70- μ m filters, processed with debris removal solution (Miltenyi Biotec), and then frozen and stored in a recovery freezing medium (Thermo Fisher Scientific). Frozen cells were thawed in 5% fetal bovine serum; sequentially stained with viability dye eFluor 450 (#65-0863-14; eBioscience), BV785 anti-human CD45 (#304048; Biolegend), BV510 anti-human CD11B (#562950; Biolegend); and processed with single-cell multiplexing kit (BD). Samples were also stained with APC anti-human TREM2 (#FAB17291A; R&D) for the downstream analysis. CD45⁺CD11B⁺ cells were sorted and loaded into the BD Rhapsody single-cell analysis system. The cDNA libraries were prepared using BD Rhapsody whole transcriptome analysis amplification kit.

Agilent DNA 4200 TapeStation assay was used for quality control. Libraries were pooled and sequenced to target 50,000

unique reads per cell using an Illumina NextSeq (high run type) for mice and an Illumina NovaSeq6000 (S1 flow cell) for humans, and with the read length of 75 base pairs and paired end.

Analysis of *de novo* scRNA-seq data

Mouse and human raw sequencing data were initially processed with Cell Ranger pipelines for 10 \times Genomics and Seven Bridges pipelines for BD Rhapsody, respectively. Briefly, FASTQ files were generated by demultiplexing and further aligned to the mouse genome reference mm10 and the human genome reference GRCh38, respectively. Feature barcode processing and unique molecular identifier (UMI) counting were then performed according to the standard workflow. The following criteria were applied as quality control using Seurat (Hao et al., 2021; v4): cells that had <200 UMI counts or genes that were expressed by fewer than three cells were removed from further analysis. Mouse cells that had >5,000 UMI counts or >20% of mitochondrial genes were also excluded, while doublets of human cells were identified and removed after clustering analysis.

Data integration was performed using Seurat (Hao et al., 2021). Specifically, the mouse datasets were integrated with a previously published retinal microglial dataset from the LD model (O'Koren et al., 2019), and the datasets of the human neuroretina and RPE/choroids were also integrated before clustering analysis. After filtering, the top 2,500 and 2,000 features were selected to identify the anchors for mouse and human datasets, respectively. The top 30 principal components (PCs) were used to generate Uniform Manifold Approximation and Projection (UMAP) clustering. To identify the conserved marker genes of subretinal microglia in mice, differential gene analysis was performed in each model and then the overlapped markers were selected.

Gene module scores of homeostatic microglia, subretinal microglia, perivascular macrophages, and monocyte-derived macrophages were calculated as previously described (Tirosh et al., 2016). For each population, the top 200 DEGs ranked by fold change and identified in a mouse model were used to generate the module score with AddModuleScore function in Seurat. Data were visualized with DotPlot.

Pathway enrichment analyses were performed using the top 200 shared upregulated genes that were ranked by average fold change of subretinal microglial clusters from mice and human donors. Gene ontology database with biological process was used (<http://geneontology.org>). A pathway was considered significantly overrepresented with false discovery rate < 0.05.

Integration and analysis of independent AMD scRNA-seq datasets

The scRNA-seq datasets from another two independent AMD studies were downloaded with the accession number GSE183320 (Voigt et al., 2022) and GSE203499, respectively. Clustering analysis was first performed to extract myeloid cells by *AIF1* expression in these two datasets. The myeloid cells were further integrated with our *de novo* dataset using Seurat. The top 3,000 features were used to identify the anchors for integration, and the top 30 PCs were used to generate UMAP clustering.

The label transfer was performed with the default setting of Seurat tutorial. Our *de novo* dataset was used as the reference

and the other two datasets were used as queries. The RHO^{high} cluster unique present in one AMD donor was excluded from the label transfer. Based on the metadata availability, the frequencies of subretinal microglia clusters relative to all myeloid cells in the whole or the macular RPE/choroid were calculated for each donor.

Flow cytometry analysis

Data from human RPE/choroid tissues were collected using BD FACSAria III Cell Sorter and analyzed using FlowJo software (version 10.7.2). Blood from human donors was used as controls to draw flow gating for viability, CD45⁺ and CD11B⁺ cells, respectively. CD45⁺CD11B⁻ cells from human blood were used as a negative control for gating TREM2⁺ cells in RPE/choroid tissues.

Statistical analysis

Data are presented as means \pm standard errors. Normal distribution and homogeneity of variance were tested before applying any parametric analysis, and data transformation was performed when needed. If the assumptions of a parametric test cannot fit, a non-parametric test was used. Depending on the research questions, one-tailed or two-tailed tests were used. A student's *t* test or Mann–Whitney test was used for two group comparisons. For multiple comparisons, one-way or two-way ANOVAs followed by Tukey's post-hoc test were used. For correlation analysis, Spearman's correlation coefficient was used for rank-ordered data. All non-sequencing experiments were repeated at least twice. A *P* value <0.05 is considered statistically significant. All statistical data were analyzed using GraphPad Prism.

Online supplemental material

Fig. S1, related to **Fig. 1**, shows additional scRNA-seq analysis and morphological quantifications of subretinal microglia across mouse models. **Fig. S2**, related to **Fig. 2**, shows additional data on the contributions of Gal3 to restricting disease progression in mice. **Fig. S3**, related to **Fig. 3**, shows additional evidence about regulation by Trem2 signaling in subretinal microglia. **Fig. S4**, related to **Fig. 4**, shows additional data on 4D9 treatment. **Fig. S5**, related to **Fig. 5**, shows additional scRNA-seq analysis of myeloid cells in human donors. **Fig. S6**, related to **Fig. 6**, shows additional evidence about the validation of GAL3 and TREM2 expression in human donors. Table S1 is the list of shared DEGs of subretinal microglia across mouse models. Table S2 is the metadata of human donors and eye samples. Table S3 is the list of DEGs of three retinal microglial clusters in human donors.

Data availability

Two human and mouse scRNA-seq datasets generated by this study have been deposited in the Gene Expression Omnibus (GEO) with the accession numbers GSE208434 and GSE195891, respectively. The retinal microglial dataset from the LD model is under the accession number GSE126783. The other two datasets of human AMD were downloaded with the accession numbers GSE183320 and GSE203499, respectively. All the analytic scripts are available upon request. All other data needed to evaluate the conclusions in this paper are available in the paper or the supplementary materials.

Acknowledgments

We thank Kathryn Monroe at Denali Therapeutics, South San Francisco, CA, USA, for providing the modified 4D9 antibodies. We thank Bart O. Williams for providing frozen sperms of *Lgals3^{fl/fl}* mice. We acknowledge technical assistance from Duke core facilities.

This work was supported by National Institutes of Health (NIH)/National Eye Institute (NEI) grants R01EY030906 (D.R. Saban), R01EY021798 (D.R. Saban), R01EY031748 (C. Bowes Rickman), and 5K23EY026988 (E.M. Lad), BrightFocus Foundation Macular Degeneration Research grant (D.R. Saban), Research to Prevent Blindness Elizabeth Althouse Special Scholar Award (E.M. Lad), Research to Prevent Blindness (Unrestricted, Duke Eye Center), and NIH/NEI Core grant P30EY005722 (Duke Eye Center). C. Haass is supported by the Deutsche Forschungsgemeinschaft (German Research Foundation) with the Koselleck Project HA1737/16-1.

Author contributions: C. Yu: Conceptualization, Data curation, Formal analysis, Investigation, Methodology, Resources, Software, Validation, Visualization, Writing - original draft, Writing - review & editing. E.M. Lad: Conceptualization, Funding acquisition, Investigation, Writing - review & editing. R. Mathew: Conceptualization, Data curation, Formal analysis, Investigation, Methodology, Project administration, Validation, Writing - review & editing. N. Shiraki: Investigation, Writing - review & editing. S. Littleton: Data curation, Formal analysis, Resources, Software, Writing - review & editing. Y. Chen: Resources, Writing - review & editing. J. Hou: Resources. K. Schlepckow: Conceptualization, Methodology, Resources, Writing - review & editing. S. Degan: Formal analysis, Investigation, Methodology, Writing - review & editing. L. Chew: Data curation, Formal analysis. J. Amason: Data curation, Formal analysis, Investigation, Resources. J. Kalnitsky: Data curation, Investigation, Writing - review & editing. C. Bowes Rickman: Resources, Writing - review & editing. A.D. Proia: Conceptualization, Formal analysis, Investigation, Methodology, Resources, Validation, Visualization, Writing - original draft, Writing - review & editing. M. Colonna: Resources. C. Haass: Conceptualization, Methodology, Resources, Writing - review & editing. D.R. Saban: Conceptualization, Funding acquisition, Methodology, Project administration, Supervision, Writing - original draft, Writing - review & editing.

Disclosures: C. Yu reported a patent to DU7705PROV-2 pending. K. Schlepckow and C. Haass reported "other" from Denali Therapeutics during the conduct of the study and grants from Cure Alzheimer's Fund outside the submitted work; in addition, K. Schlepckow and C. Haass had a patent to WO-2018015573-A2 issued, a patent to PTO-1382, file reference no. 123658-12002 licensed Bex Vision, Inc., and a patent to DNL-008-10-P1 - 02900.044PV1 pending; and received €1,000 inventor royalties from the German Center for Neurodegenerative Diseases for co-developing a therapeutic anti-TREM2 antibody (see Schlepckow et al., 2020). M. Colonna reported personal fees from Vigil Neuro, grants from Vigil Neuro, and personal fees from Cell Signaling Technology during the conduct of the study; in addition, M. Colonna had a patent to patent to TREM2 pending. D.R.

Saban reported a patent pending. No other disclosures were reported.

Submitted: 12 June 2023

Revised: 11 December 2023

Accepted: 12 January 2024

References

- Ajami, B., J.L. Bennett, C. Krieger, K.M. McNagny, and F.M. Rossi. 2011. Infiltrating monocytes trigger EAE progression, but do not contribute to the resident microglia pool. *Nat. Neurosci.* 14:1142–1149. <https://doi.org/10.1038/nn.2887>
- Ajami, B., J.L. Bennett, C. Krieger, W. Tetzlaff, and F.M. Rossi. 2007. Local self-renewal can sustain CNS microglia maintenance and function throughout adult life. *Nat. Neurosci.* 10:1538–1543. <https://doi.org/10.1038/nn2014>
- Anderson, S.R., J.M. Roberts, J. Zhang, M.R. Steele, C.O. Romero, A. Bosco, and M.L. Vetter. 2019. Developmental apoptosis promotes a disease-related gene signature and independence from CSF1R signaling in retinal microglia. *Cell Rep.* 27:2002–2013.e15. <https://doi.org/10.1016/j.celrep.2019.04.062>
- Badimon, A., H.J. Strasburger, P. Ayata, X. Chen, A. Nair, A. Ikegami, P. Hwang, A.T. Chan, S.M. Graves, J.O. Uweru, et al. 2020. Negative feedback control of neuronal activity by microglia. *Nature.* 586:417–423. <https://doi.org/10.1038/s41586-020-2777-8>
- Beguier, F., M. Housset, C. Roubeix, S. Augustin, Y. Zagar, C. Nous, T. Mathis, C. Eandi, M. Benchaboune, A. Drame-Maigné, et al. 2020. The 10q26 risk haplotype of age-related macular degeneration aggravates subretinal inflammation by impairing monocyte elimination. *Immunity.* 53:429–441.e8. <https://doi.org/10.1016/j.immuni.2020.07.021>
- Bennett, F.C., M.L. Bennett, F. Yaqoob, S.B. Mulinyawe, G.A. Grant, M. Hayden Gephart, E.D. Plowey, and B.A. Barres. 2018. A combination of ontogeny and CNS environment establishes microglial identity. *Neuron.* 98:1170–1183.e8. <https://doi.org/10.1016/j.neuron.2018.05.014>
- Boza-Serrano, A., R. Ruiz, R. Sanchez-Varo, J. Garcia-Revilla, Y. Yang, I. Jimenez-Ferrer, A. Paulus, M. Wennström, A. Vilalta, D. Allendorf, et al. 2019. Galectin-3, a novel endogenous TREM2 ligand, detrimentally regulates inflammatory response in Alzheimer's disease. *Acta Neuropathol.* 138:251–273. <https://doi.org/10.1007/s00401-019-02013-z>
- Butovsky, O., M.P. Jedrychowski, C.S. Moore, R. Cialic, A.J. Lanser, G. Gabriely, T. Koeglsparger, B. Dake, P.M. Wu, C.E. Doykan, et al. 2014. Identification of a unique TGF- β -dependent molecular and functional signature in microglia. *Nat. Neurosci.* 17:131–143. <https://doi.org/10.1038/nn.3599>
- Buttgereit, A., I. Lelios, X. Yu, M. Vrohings, N.R. Krakoski, E.L. Gautier, R. Nishinakamura, B. Becher, and M. Greter. 2016. Sall1 is a transcriptional regulator defining microglia identity and function. *Nat. Immunol.* 17:1397–1406. <https://doi.org/10.1038/ni.3585>
- Calippe, B., S. Augustin, F. Beguier, H. Charles-Messance, L. Poupel, J.B. Conart, S.J. Hu, S. Lavalette, A. Fauvet, J. Rayes, et al. 2017. Complement factor H inhibits CD47-mediated resolution of inflammation. *Immunity.* 46:261–272. <https://doi.org/10.1016/j.immuni.2017.01.006>
- Combadière, C., C. Feumi, W. Raoul, N. Keller, M. Rodéro, A. Pézard, S. Lavalette, M. Houssier, L. Jonet, E. Picard, et al. 2007. CX3CR1-dependent subretinal microglia cell accumulation is associated with cardinal features of age-related macular degeneration. *J. Clin. Invest.* 117:2920–2928. <https://doi.org/10.1172/JCI31692>
- Cronk, J.C., A.J. Filiano, A. Louveau, I. Marin, R. Marsh, E. Ji, D.H. Goldman, I. Smirnov, N. Geraci, S. Acton, et al. 2018. Peripherally derived macrophages can engraft the brain independent of irradiation and maintain an identity distinct from microglia. *J. Exp. Med.* 215:1627–1647. <https://doi.org/10.1084/jem.20180247>
- Day, W.A., M.R. Lefever, R.L. Ochs, A. Pedata, L.J. Behman, J. Ashworth-Sharp, D.D. Johnson, E.J. May, J.G. Grille, E.A. Roberts, et al. 2017. Covalently deposited dyes: A new chromogen paradigm that facilitates analysis of multiple biomarkers in situ. *Lab. Invest.* 97:104–113. <https://doi.org/10.1038/labinvest.2016.115>
- De Biase, L.M., K.E. Schuebel, Z.H. Füsfield, K. Jair, I.A. Hawes, R. Cimbrow, H.Y. Zhang, Q.R. Liu, H. Shen, Z.X. Xi, et al. 2017. Local cues establish and maintain region-specific phenotypes of basal ganglia microglia. *Neuron.* 95:341–356.e6. <https://doi.org/10.1016/j.neuron.2017.06.020>
- Doyle, S.L., M. Campbell, E. Ozaki, R.G. Salomon, A. Mori, P.F. Kenna, G.J. Farrar, A.S. Kiang, M.M. Humphries, E.C. Lavelle, et al. 2012. NLRP3 has a protective role in age-related macular degeneration through the induction of IL-18 by drusen components. *Nat. Med.* 18:791–798. <https://doi.org/10.1038/nm.2717>
- Ennerfelt, H., E.L. Frost, D.A. Shapiro, C. Holliday, K.E. Zengeler, G. Voithofer, A.C. Bolte, C.R. Lammert, J.A. Kulas, T.K. Ulland, and J.R. Lukens. 2022. SYK coordinates neuroprotective microglial responses in neurodegenerative disease. *Cell.* 185:4135–4152.e22. <https://doi.org/10.1016/j.cell.2022.09.030>
- Esposito, N.J., F. Mazzoni, J.A. Vargas, and S.C. Finnemann. 2021. Diurnal photoreceptor outer segment renewal in mice is independent of galectin-3. *Invest. Ophthalmol. Vis. Sci.* 62:7. <https://doi.org/10.1167/iov.62.2.7>
- Ewers, M., N. Franzmeier, M. Suarez-Calvet, E. Morenas-Rodriguez, M.A.A. Caballero, G. Kleinberger, L. Piccio, C. Cruchaga, Y. Deming, M. Dichgans, et al. 2019. Increased soluble TREM2 in cerebrospinal fluid is associated with reduced cognitive and clinical decline in Alzheimer's disease. *Sci. Transl. Med.* 11:eaav6221. <https://doi.org/10.1126/scitranslmed.aav6221>
- Fahrenhold, M., S. Rakic, J. Classey, C. Brayne, P.G. Ince, J.A.R. Nicoll, D. Boche, and MRC-CFAS. 2018. TREM2 expression in the human brain: A marker of monocyte recruitment? *Brain Pathol.* 28:595–602. <https://doi.org/10.1111/bpa.12564>
- Fritsche, L.G., W. Igl, J.N. Bailey, F. Grassmann, S. Sengupta, J.L. Bragg-Gresham, K.P. Burdon, S.J. Hebbaring, C. Wen, M. Gorski, et al. 2016. A large genome-wide association study of age-related macular degeneration highlights contributions of rare and common variants. *Nat. Genet.* 48:134–143. <https://doi.org/10.1038/ng.3448>
- Ginhoux, F., M. Greter, M. Leboeuf, S. Nandi, P. See, S. Gokhan, M.F. Mehler, S.J. Conway, L.G. Ng, E.R. Stanley, et al. 2010. Fate mapping analysis reveals that adult microglia derive from primitive macrophages. *Science.* 330:841–845. <https://doi.org/10.1126/science.1194637>
- Grabert, K., T. Michoel, M.H. Karavolos, S. Clohisey, J.K. Baillie, M.P. Stevens, T.C. Freeman, K.M. Summers, and B.W. McColl. 2016. Microglial brain region-dependent diversity and selective regional sensitivities to aging. *Nat. Neurosci.* 19:504–516. <https://doi.org/10.1038/nn.4222>
- Greferath, U., R.H. Guymner, K.A. Vessey, K. Brassington, and E.L. Fletcher. 2016. Correlation of histologic features with in vivo imaging of reticular pseudodrusen. *Ophthalmology.* 123:1320–1331. <https://doi.org/10.1016/j.ophtha.2016.02.009>
- Gupta, N., K.E. Brown, and A.H. Milam. 2003. Activated microglia in human retinitis pigmentosa, late-onset retinal degeneration, and age-related macular degeneration. *Exp. Eye Res.* 76:463–471. [https://doi.org/10.1016/S0014-4835\(02\)00332-9](https://doi.org/10.1016/S0014-4835(02)00332-9)
- Hageman, G.S., P.J. Luthert, N.H. Victor Chong, L.V. Johnson, D.H. Anderson, and R.F. Mullins. 2001. An integrated hypothesis that considers drusen as biomarkers of immune-mediated processes at the RPE-Bruch's membrane interface in aging and age-related macular degeneration. *Prog. Retin. Eye Res.* 20:705–732. [https://doi.org/10.1016/S1350-9462\(01\)00010-6](https://doi.org/10.1016/S1350-9462(01)00010-6)
- Hammond, T.R., C. Dufort, L. Dissing-Olesen, S. Giera, A. Young, A. Wysoker, A.J. Walker, F. Gergits, M. Segel, J. Nemes, et al. 2019. Single-cell RNA sequencing of microglia throughout the mouse lifespan and in the injured brain reveals complex cell-state changes. *Immunity.* 50:253–271.e6. <https://doi.org/10.1016/j.immuni.2018.11.004>
- Hao, Y., S. Hao, E. Andersen-Nissen, W.M. Mauck III, S. Zheng, A. Butler, M.J. Lee, A.J. Wilk, C. Darby, M. Zager, et al. 2021. Integrated analysis of multimodal single-cell data. *Cell.* 184:3573–3587.e29. <https://doi.org/10.1016/j.cell.2021.04.048>
- Hesgrave, A., W. Heywood, R. Paterson, N. Magdalinou, J. Svensson, P. Johansson, A. Öhrfelt, K. Blennow, J. Hardy, J. Schott, et al. 2016. Increased cerebrospinal fluid soluble TREM2 concentration in Alzheimer's disease. *Mol. Neurodegener.* 11:3. <https://doi.org/10.1186/s13024-016-0071-x>
- Hsieh, C.L., M. Koike, S.C. Spusta, E.C. Niemi, M. Yenari, M.C. Nakamura, and W.E. Seaman. 2009. A role for TREM2 ligands in the phagocytosis of apoptotic neuronal cells by microglia. *J. Neurochem.* 109:1144–1156. <https://doi.org/10.1111/j.1471-4159.2009.06042.x>
- Jakobiec, F.A., P.C. Barrantes, Y. Yonekawa, E.M. Lad, and A.D. Proia. 2021. Subretinal mononuclear cells in coats' disease studied with RPE65 and CD163: Evidence for histiocytoid pigment epithelial cells. *Am. J. Ophthalmol.* 222:388–396. <https://doi.org/10.1016/j.ajo.2020.09.020>
- Kana, V., F.A. Desland, M. Casanova-Acebes, P. Ayata, A. Badimon, E. Nabel, K. Yamamuro, M. Sneboer, I.L. Tan, M.E. Flanagan, et al. 2019. CSF-

- 1 controls cerebellar microglia and is required for motor function and social interaction. *J. Exp. Med.* 216:2265–2281. <https://doi.org/10.1084/jem.20182037>
- Keren-Shaul, H., A. Spinrad, A. Weiner, O. Matcovitch-Natan, R. Dvir-Szternfeld, T.K. Ulland, E. David, K. Baruch, D. Lara-Astaiso, B. Toth, et al. 2017. A unique microglia type associated with restricting development of Alzheimer's disease. *Cell*. 169:1276–1290.e17. <https://doi.org/10.1016/j.cell.2017.05.018>
- Kerur, N., S. Fukuda, D. Banerjee, Y. Kim, D. Fu, I. Apicella, A. Varshney, R. Yasuma, B.J. Fowler, E. Baghdasaryan, et al. 2018. cGAS drives noncanonical-inflammasome activation in age-related macular degeneration. *Nat. Med.* 24:50–61. <https://doi.org/10.1038/nm.4450>
- Kohno, H., Y. Chen, B.M. Kevany, E. Pearlman, M. Miyagi, T. Maeda, K. Palczewski, and A. Maeda. 2013. Photoreceptor proteins initiate microglial activation via Toll-like receptor 4 in retinal degeneration mediated by all-trans-retinal. *J. Biol. Chem.* 288:15326–15341. <https://doi.org/10.1074/jbc.M112.448712>
- Krasemann, S., C. Madore, R. Cialic, C. Baufeld, N. Calcagno, R. El Fatimy, L. Beckers, E. O'Loughlin, Y. Xu, Z. Fanek, et al. 2017. The TREM2-APOE pathway drives the transcriptional phenotype of dysfunctional microglia in neurodegenerative diseases. *Immunity*. 47:566–581.e9. <https://doi.org/10.1016/j.immuni.2017.08.008>
- Lad, E.M., S.W. Cousins, J.S. Van Arnam, and A.D. Proia. 2015. Abundance of infiltrating CD163+ cells in the retina of postmortem eyes with dry and neovascular age-related macular degeneration. *Graefes Arch. Clin. Exp. Ophthalmol.* 253:1941–1945. <https://doi.org/10.1007/s00417-015-3094-z>
- Lee, C.Y.D., A. Daggett, X. Gu, L.L. Jiang, P. Langfelder, X. Li, N. Wang, Y. Zhao, C.S. Park, Y. Cooper, et al. 2018. Elevated TREM2 gene dosage reprograms microglia reactivity and ameliorates pathological phenotypes in Alzheimer's disease models. *Neuron*. 97:1032–1048.e5. <https://doi.org/10.1016/j.neuron.2018.02.002>
- Levy, O., S. Lavalette, S.J. Hu, M. Housset, W. Raoul, C. Eandi, J.A. Sahel, P.M. Sullivan, X. Guillonnet, and F. Sennlaub. 2015. APOE isoforms control pathogenic subretinal inflammation in age-related macular degeneration. *J. Neurosci.* 35:13568–13576. <https://doi.org/10.1523/JNEUROSCI.2468-15.2015>
- Lew, D.S., M.J. McGrath, and S.C. Finnemann. 2022. Galectin-3 promotes müller glia clearance phagocytosis via MERTK and reduces harmful müller glia activation in inherited and induced retinal degeneration. *Front. Cell. Neurosci.* 16:878260. <https://doi.org/10.3389/fncel.2022.878260>
- Ma, X., Y. Takahashi, W. Wu, W. Liang, J. Chen, D. Chakraborty, Y. Li, Y. Du, S. Benyajati, and J.X. Ma. 2021. ADAM17 mediates ectodomain shedding of the soluble VLDL receptor fragment in the retinal epithelium. *J. Biol. Chem.* 297:101185. <https://doi.org/10.1016/j.jbc.2021.101185>
- Margeta, M.A., Z. Yin, C. Madore, K.M. Pitts, S.M. Letcher, J. Tang, S. Jiang, C.D. Gauthier, S.R. Silveira, C.M. Schroeder, et al. 2022. Apolipoprotein E4 impairs the response of neurodegenerative retinal microglia and prevents neuronal loss in glaucoma. *Immunity*. 55:1627–1644.e7. <https://doi.org/10.1016/j.immuni.2022.07.014>
- Maupin, K.A., K. Weaver, A. Bergsma, C. Christie, Z.A. Zhong, T. Yang, and B.O. Williams. 2018. Enhanced cortical bone expansion in Lgals3-deficient mice during aging. *Bone Res.* 6:7. <https://doi.org/10.1038/s41413-017-0003-6>
- Mazaheri, F., N. Snaidero, G. Kleinberger, C. Madore, A. Daria, G. Werner, S. Krasemann, A. Capell, D. Trümbach, W. Wurst, et al. 2017. TREM2 deficiency impairs chemotaxis and microglial responses to neuronal injury. *EMBO Rep.* 18:1186–1198. <https://doi.org/10.15252/embr.201743922>
- Mehina, E.M.F., S. Taylor, R. Boghozian, E. White, S.E. Choi, M.S. Cheema, J. Korbelin, and C.E. Brown. 2021. Invasion of phagocytic Galectin 3 expressing macrophages in the diabetic brain disrupts vascular repair. *Sci. Adv.* 7:eabg2712. <https://doi.org/10.1126/sciadv.abg2712>
- Mildner, A., H. Schmidt, M. Nitsche, D. Merkler, U.K. Hanisch, M. Mack, M. Heikenwalder, W. Bruck, J. Priller, and M. Prinz. 2007. Microglia in the adult brain arise from Ly-6ChiCCR2+ monocytes only under defined host conditions. *Nat. Neurosci.* 10:1544–1553. <https://doi.org/10.1038/nn2015>
- Molgora, M., E. Esaulova, W. Vermi, J. Hou, Y. Chen, J. Luo, S. Brioschi, M. Bugatti, A.S. Omodei, B. Ricci, et al. 2020. TREM2 modulation remodels the tumor myeloid landscape enhancing anti-PD-1 immunotherapy. *Cell*. 182:886–900.e17. <https://doi.org/10.1016/j.cell.2020.07.013>
- Morenas-Rodríguez, E., Y. Li, B. Nuscher, N. Franzmeier, C. Xiong, M. Suárez-Calvet, A.M. Fagan, S. Schultz, B.A. Gordon, T.L.S. Benzinger, et al. 2022. Soluble TREM2 in CSF and its association with other biomarkers and cognition in autosomal-dominant Alzheimer's disease: A longitudinal observational study. *Lancet Neurol.* 21:329–341. [https://doi.org/10.1016/S1474-4422\(22\)00027-8](https://doi.org/10.1016/S1474-4422(22)00027-8)
- Nugent, A.A., K. Lin, B. van Lengerich, S. Lianoglou, L. Przybyla, S.S. Davis, C. Llapashtica, J. Wang, D.J. Kim, D. Xia, et al. 2020. TREM2 regulates microglial cholesterol metabolism upon chronic phagocytic challenge. *Neuron*. 105:837–854.e9. <https://doi.org/10.1016/j.neuron.2019.12.007>
- O'Koren, E.G., R. Mathew, and D.R. Saban. 2016. Fate mapping reveals that microglia and recruited monocyte-derived macrophages are definitively distinguishable by phenotype in the retina. *Sci. Rep.* 6:20636. <https://doi.org/10.1038/srep20636>
- O'Koren, E.G., C. Yu, M. Klingeborn, A.Y.W. Wong, C.L. Prigge, R. Mathew, J. Kalnitsky, R.A. Msallam, A. Silvin, J.N. Kay, et al. 2019. Microglial function is distinct in different anatomical locations during retinal homeostasis and degeneration. *Immunity*. 50:723–737.e7. <https://doi.org/10.1016/j.immuni.2019.02.007>
- O'Malley, P., R.A. Allen, B.R. Straatsma, and C.C. O'Malley. 1965. Paving-stone degeneration of the retina. *Arch. Ophthalmol.* 73:169–182. <https://doi.org/10.1001/archophth.1965.00970030171006>
- O'Malley, P.F., and R.A. Allen. 1967. Peripheral cystoid degeneration of the retina. Incidence and distribution in 1,000 autopsy eyes. *Arch. Ophthalmol.* 77:769–776. <https://doi.org/10.1001/archophth.1967.00980020771010>
- Parhizkar, S., T. Arzberger, M. Brendel, G. Kleinberger, M. Deussing, C. Focke, B. Nuscher, M. Xiong, A. Ghasemigharagoz, N. Katzmarzki, et al. 2019. Loss of TREM2 function increases amyloid seeding but reduces plaque-associated ApoE. *Nat. Neurosci.* 22:191–204. <https://doi.org/10.1038/s41593-018-0296-9>
- Park, G.B., D. Kim, Y.S. Kim, J.W. Kim, H. Sun, K.H. Roh, J.W. Yang, and D.Y. Hur. 2015. Regulation of ADAM10 and ADAM17 by sorafenib inhibits epithelial-to-mesenchymal transition in epstein-barr virus-infected retinal pigment epithelial cells. *Invest. Ophthalmol. Vis. Sci.* 56:5162–5173. <https://doi.org/10.1167/iovs.14-16058>
- Piccio, L., Y. Deming, J.L. Del-Aguila, L. Ghezzi, D.M. Holtzman, A.M. Fagan, C. Fenoglio, D. Galimberti, B. Borroni, and C. Cruchaga. 2016. Cerebrospinal fluid soluble TREM2 is higher in Alzheimer disease and associated with mutation status. *Acta Neuropathol.* 131:925–933. <https://doi.org/10.1007/s00401-016-1533-5>
- Prokop, S., K.R. Miller, N. Drost, S. Handrick, V. Mathur, J. Luo, A. Wegner, T. Wyss-Coray, and F.L. Heppner. 2015. Impact of peripheral myeloid cells on amyloid- β pathology in Alzheimer's disease-like mice. *J. Exp. Med.* 212:1811–1818. <https://doi.org/10.1084/jem.20150479>
- Rashid, K., I. Akhtar-Schaefer, and T. Langmann. 2019. Microglia in retinal degeneration. *Front. Immunol.* 10:1975. <https://doi.org/10.3389/fimmu.2019.01975>
- Reed-Geaghan, E.G., A.L. Croxford, B. Becher, and G.E. Landreth. 2020. Plaque-associated myeloid cells derive from resident microglia in an Alzheimer's disease model. *J. Exp. Med.* 217:e20191374. <https://doi.org/10.1084/jem.20191374>
- Sakami, S., T. Maeda, G. Bereta, K. Okano, M. Golczak, A. Sumaroka, A.J. Roman, A.V. Cideciyan, S.G. Jacobson, and K. Palczewski. 2011. Probing mechanisms of photoreceptor degeneration in a new mouse model of the common form of autosomal dominant retinitis pigmentosa due to P23H opsin mutations. *J. Biol. Chem.* 286:10551–10567. <https://doi.org/10.1074/jbc.M110.209759>
- Satoh, J., N. Kawana, Y. Yamamoto, T. Ishida, Y. Saito, and K. Arima. 2013. A survey of TREM2 antibodies reveals neuronal but not microglial staining in formalin-fixed paraffin-embedded postmortem Alzheimer's brain tissues. *Alzheimers Res. Ther.* 5:30. <https://doi.org/10.1186/alzrt184>
- Saylor, J., Z. Ma, H.S. Goodridge, F. Huang, A.E. Cress, S.J. Pandol, S.L. Shiao, A.C. Vidal, L. Wu, N.G. Nickols, et al. 2018. Spatial mapping of myeloid cells and macrophages by multiplexed tissue staining. *Front. Immunol.* 9:2925. <https://doi.org/10.3389/fimmu.2018.02925>
- Schleppckow, K., K.M. Monroe, G. Kleinberger, L. Cantuti-Castelvetri, S. Parhizkar, D. Xia, M. Willem, G. Werner, N. Pettkus, B. Brunner, et al. 2020. Enhancing protective microglial activities with a dual function TREM2 antibody to the stalk region. *EMBO Mol. Med.* 12:e11227. <https://doi.org/10.15252/emmm.201911227>
- Sennlaub, F., C. Auvynet, B. Calippe, S. Lavalette, L. Poupel, S.J. Hu, E. Dominguez, S. Camelo, O. Levy, E. Guyon, et al. 2013. CCR2(+) monocytes infiltrate atrophic lesions in age-related macular disease and mediate photoreceptor degeneration in experimental subretinal inflammation in Cx3cr1 deficient mice. *EMBO Mol. Med.* 5:1775–1793. <https://doi.org/10.1002/emmm.201302692>
- Shemer, A., J. Grozovski, T.L. Tay, J. Tao, A. Volaski, P. Süß, A. Ardura-Fabregat, M. Gross-Vered, J.S. Kim, E. David, et al. 2018. Engrafted

- parenchymal brain macrophages differ from microglia in transcriptome, chromatin landscape and response to challenge. *Nat. Commun.* 9:5206. <https://doi.org/10.1038/s41467-018-07548-5>
- Siew, J.J., H.M. Chen, H.Y. Chen, H.L. Chen, C.M. Chen, B.W. Soong, Y.R. Wu, C.P. Chang, Y.C. Chan, C.H. Lin, et al. 2019. Galectin-3 is required for the microglia-mediated brain inflammation in a model of Huntington's disease. *Nat. Commun.* 10:3473. <https://doi.org/10.1038/s41467-019-11441-0>
- Silverman, S.M., W. Ma, X. Wang, L. Zhao, and W.T. Wong. 2019. C3- and CR3-dependent microglial clearance protects photoreceptors in retinitis pigmentosa. *J. Exp. Med.* 216:1925–1943. <https://doi.org/10.1084/jem.20190009>
- Sirko, S., M. Irmeler, S. Gascón, S. Bek, S. Schneider, L. Dimou, J. Obermann, D. De Souza Paiva, F. Poirier, J. Beckers, et al. 2015. Astrocyte reactivity after brain injury—: The role of galectins 1 and 3. *Glia.* 63:2340–2361. <https://doi.org/10.1002/glia.22898>
- Sorsby, A. 1941. Experimental pigmentary degeneration of the retina by sodium iodate. *Br. J. Ophthalmol.* 25:58–62. <https://doi.org/10.1136/bjo.25.2.58>
- Suárez-Calvet, M., M.A. Araque Caballero, G. Kleinberger, R.J. Bateman, A.M. Fagan, J.C. Morris, J. Levin, A. Danek, M. Ewers, C. Haass, et al. 2016a. Early changes in CSF sTREM2 in dominantly inherited Alzheimer's disease occur after amyloid deposition and neuronal injury. *Sci. Transl. Med.* 8:369ra178. <https://doi.org/10.1126/scitranslmed.aag1767>
- Suárez-Calvet, M., G. Kleinberger, M.A. Araque Caballero, M. Brendel, A. Rominger, D. Alcolea, J. Fortea, A. Lleó, R. Blesa, J.D. Gispert, et al. 2016b. sTREM2 cerebrospinal fluid levels are a potential biomarker for microglia activity in early-stage Alzheimer's disease and associate with neuronal injury markers. *EMBO Mol. Med.* 8:466–476. <https://doi.org/10.15252/emmm.201506123>
- Tabel, M., A. Wolf, M. Szczepan, H. Xu, H. Jäggle, C. Moehle, M. Chen, and T. Langmann. 2022. Genetic targeting or pharmacological inhibition of galectin-3 dampens microglia reactivity and delays retinal degeneration. *J. Neuroinflammation.* 19:229. <https://doi.org/10.1186/s12974-022-02589-6>
- Tang, P.H., M.J. Pierson, N.D. Heuss, and D.S. Gregerson. 2017. A subpopulation of activated retinal macrophages selectively migrated to regions of cone photoreceptor stress, but had limited effect on cone death in a mouse model for type 2 Leber congenital amaurosis. *Mol. Cell. Neurosci.* 85:70–81. <https://doi.org/10.1016/j.mcn.2017.09.002>
- Tao, C.C., K.M. Cheng, Y.L. Ma, W.L. Hsu, Y.C. Chen, J.L. Fuh, W.J. Lee, C.C. Chao, and E.H.Y. Lee. 2020. Galectin-3 promotes A β oligomerization and A β toxicity in a mouse model of Alzheimer's disease. *Cell Death Differ.* 27:192–209. <https://doi.org/10.1038/s41418-019-0348-z>
- Tarallo, V., Y. Hirano, B.D. Gelfand, S. Dridi, N. Kerur, Y. Kim, W.G. Cho, H. Kaneko, B.J. Fowler, S. Bogdanovich, et al. 2012. DICER1 loss and Alu RNA induce age-related macular degeneration via the NLRP3 inflammasome and MyD88. *Cell.* 149:847–859. <https://doi.org/10.1016/j.cell.2012.03.036>
- Tirosh, I., B. Izar, S.M. Prakadan, M.H. Wadsworth II, D. Treacy, J.J. Trombetta, A. Rotem, C. Rodman, C. Lian, G. Murphy, et al. 2016. Dissecting the multicellular ecosystem of metastatic melanoma by single-cell RNA-seq. *Science.* 352:189–196. <https://doi.org/10.1126/science.aad0501>
- Turnbull, I.R., S. Gilfillan, M. Cella, T. Aoshi, M. Miller, L. Piccio, M. Hernandez, and M. Colonna. 2006. Cutting edge: TREM-2 attenuates macrophage activation. *J. Immunol.* 177:3520–3524. <https://doi.org/10.4049/jimmunol.177.6.3520>
- Uehara, F., N. Ohba, and M. Ozawa. 2001. Isolation and characterization of galectins in the mammalian retina. *Invest. Ophthalmol. Vis. Sci.* 42:2164–2172.
- Varvel, N.H., S.A. Grathwohl, K. Degenhardt, C. Resch, A. Bosch, M. Jucker, and J.J. Neher. 2015. Replacement of brain-resident myeloid cells does not alter cerebral amyloid- β deposition in mouse models of Alzheimer's disease. *J. Exp. Med.* 212:1803–1809. <https://doi.org/10.1084/jem.20150478>
- Voigt, A.P., N.K. Mullin, K. Mulfaul, L.P. Lozano, L.A. Wiley, M.J. Flamme-Wiese, E.A. Boese, I.C. Han, T.E. Scheetz, E.M. Stone, et al. 2022. Choroidal endothelial and macrophage gene expression in atrophic and neovascular macular degeneration. *Hum. Mol. Genet.* 31:2406–2423. <https://doi.org/10.1093/hmg/ddac043>
- Wang, S., R. Sudan, V. Peng, Y. Zhou, S. Du, C.M. Yuede, T. Lei, J. Hou, Z. Cai, M. Cella, et al. 2022. TREM2 drives microglia response to amyloid- β via SYK-dependent and -independent pathways. *Cell.* 185:4153–4169.e19. <https://doi.org/10.1016/j.cell.2022.09.033>
- Wang, Y., M. Cella, K. Mallinson, J.D. Ulrich, K.L. Young, M.L. Robinette, S. Gilfillan, G.M. Krishnan, S. Sudhakar, B.H. Zinselmeyer, et al. 2015. TREM2 lipid sensing sustains the microglial response in an Alzheimer's disease model. *Cell.* 160:1061–1071. <https://doi.org/10.1016/j.cell.2015.01.049>
- Wolter, J.R., and W.W. Wilson. 1959. Degeneration of the peripheral retina; report of an instructive case. *Am. J. Ophthalmol.* 47:153–166. [https://doi.org/10.1016/S0002-9394\(14\)76416-5](https://doi.org/10.1016/S0002-9394(14)76416-5)
- Wong, W.L., X. Su, X. Li, C.M. Cheung, R. Klein, C.Y. Cheng, and T.Y. Wong. 2014. Global prevalence of age-related macular degeneration and disease burden projection for 2020 and 2040: A systematic review and meta-analysis. *Lancet Glob. Health.* 2:e106–e116. [https://doi.org/10.1016/S2214-109X\(13\)70145-1](https://doi.org/10.1016/S2214-109X(13)70145-1)
- Yamasaki, R., H. Lu, O. Butovsky, N. Ohno, A.M. Rietsch, R. Cialic, P.M. Wu, C.E. Doykan, J. Lin, A.C. Cotleur, et al. 2014. Differential roles of microglia and monocytes in the inflamed central nervous system. *J. Exp. Med.* 211:1533–1549. <https://doi.org/10.1084/jem.20132477>
- Ye, C., Q. Zhou, X. Wu, C. Yu, G. Ji, D.R. Saban, and Q.Q. Li. 2020. scDAPA: detection and visualization of dynamic alternative polyadenylation from single cell RNA-seq data. *Bioinformatics.* 36:1262–1264. <https://doi.org/10.1093/bioinformatics/btz701>
- Young, K., and H. Morrison. 2018. Quantifying microglia morphology from photomicrographs of immunohistochemistry prepared tissue using ImageJ. *J. Vis. Exp.* 57648. <https://doi.org/10.3791/57648>
- Yu, C., C. Roubeix, F. Sennlaub, and D.R. Saban. 2020. Microglia versus monocytes: Distinct roles in degenerative diseases of the retina. *Trends Neurosci.* 43:433–449. <https://doi.org/10.1016/j.tins.2020.03.012>
- Zheng, H., L. Jia, C.C. Liu, Z. Rong, L. Zhong, L. Yang, X.F. Chen, J.D. Fryer, X. Wang, Y.W. Zhang, et al. 2017. TREM2 promotes microglial survival by activating Wnt/ β -Catenin pathway. *J. Neurosci.* 37:1772–1784. <https://doi.org/10.1523/JNEUROSCI.2459-16.2017>

Supplemental material

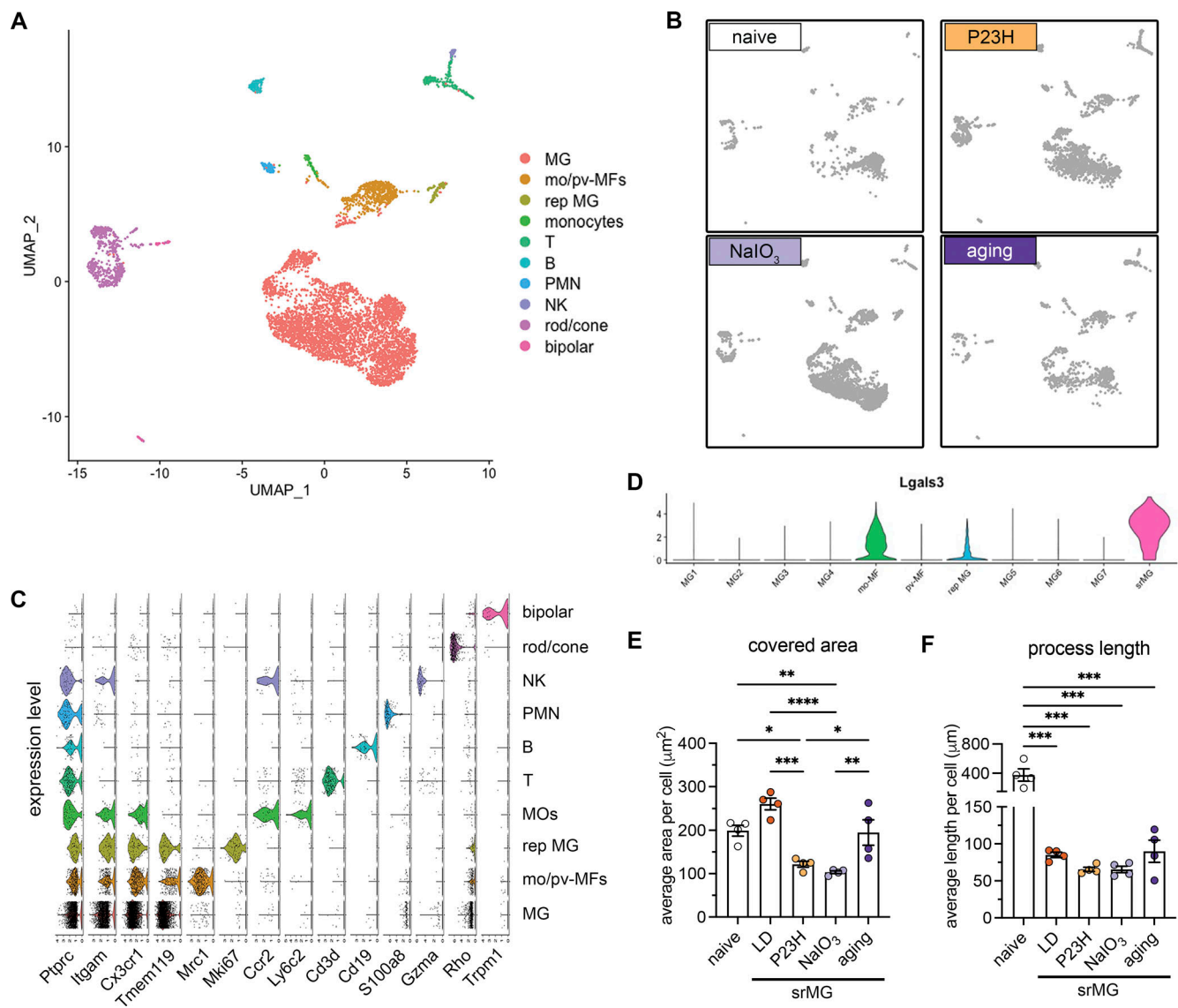


Figure S1. **scRNA-seq and morphological analysis of subretinal microglia across mouse models of outer retinal degeneration.** (A and B) UMAP plots showing retinal CD45⁺ cells collected from naïve mice, NaIO₃ mediated RPE injury model, P23H model, and advanced aging model as indicated. MG, microglia; mo-MFs, monocyte-derived macrophages; pv-MFs: perivascular macrophages; mo-DCs, monocyte-derived dendritic cells; PMN, polymorphonuclear neutrophils; NK, natural killer. (C) Violin plots show marker expressions for each cluster. (D) Violin plots showing *Lgals3* expression across all macrophage clusters. srMG, subretinal microglia. (E and F) Quantifications of covered area and process length in naïve microglia from the inner retina and subretinal microglia from four mouse models of retinal degenerations (*n* = 4 mice per group). Data were collected from two independent experiments for sequencing and validation. *: *P* < 0.05; **: *P* < 0.01; ***: *P* < 0.001; ****: *P* < 0.0001 (one-way ANOVA with Tukey's post hoc test).

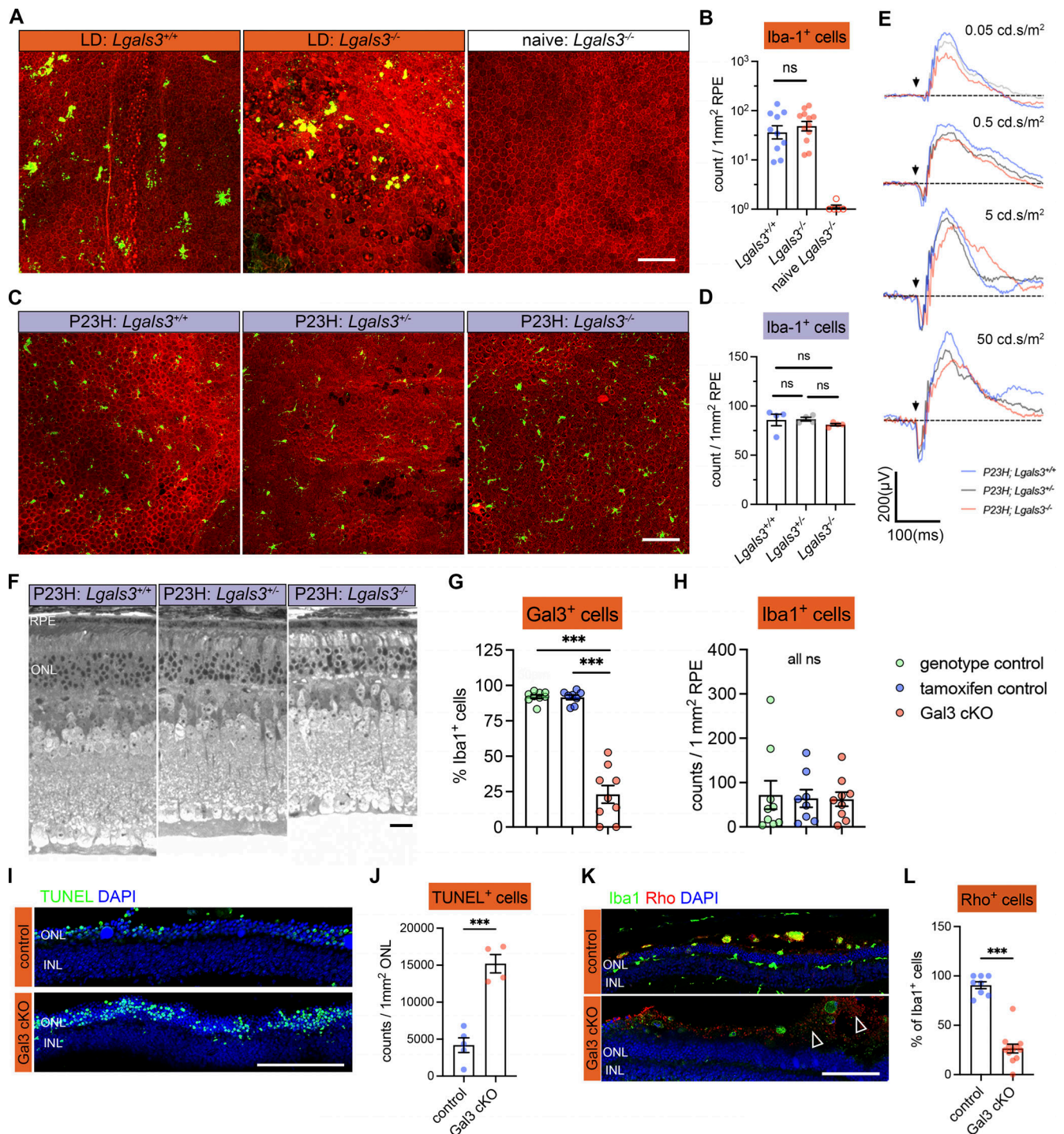


Figure S2. **Contributions of Gal3 to disease-related retinal pathology and to Iba1⁺ cell abundance in the subretinal space.** (A) Iba1 (green) and phalloidin (red) staining in RPE flatmounts from LD-subjected mice as indicated. (B) Quantifications of subretinal Iba1⁺ cells shown in A. (C) Iba1 (green) and phalloidin (red) staining in RPE flatmounts from P23H mice as indicated. (D) Quantifications of subretinal Iba1⁺ cells as shown in C. (E) Examples of ERG responses at different flash intensities as indicated. (F) Representative retinal cross-sections of WT, *Lgals3*^{+/-}, and *Lgals3*^{-/-} in P23H mice. (G and H) Quantifications of Gal3 depletion efficiency (G) and frequencies of subretinal Iba1⁺ cells (H) in Gal3 cKO mice (*n* = 9) compared with genotype control mice (*n* = 9) and tamoxifen control (*n* = 8). (I) TUNEL (green) and DAPI (blue) staining in control and Gal3 cKO retinal cross-sections in LD. INL, inner nuclear layer. (J) Quantifications of TUNEL⁺ photoreceptors in ONL (*n* = 4 per group). (K) Rhodopsin (red) and Iba1 (green) staining in control and Gal3 cKO retinal cross-sections in LD. Images from single planes of confocal scans were shown. (L) Quantifications of rhodopsin⁺ subretinal microglia. Dots represent the percentage of each image. Scale bars: 100 μm. Data were collected from two to three independent experiments. ***: *P* < 0.001; ns: not significant. One-way ANOVA with Tukey's post hoc test (B, D, G, and H); unpaired Student's *t* test (J and L).

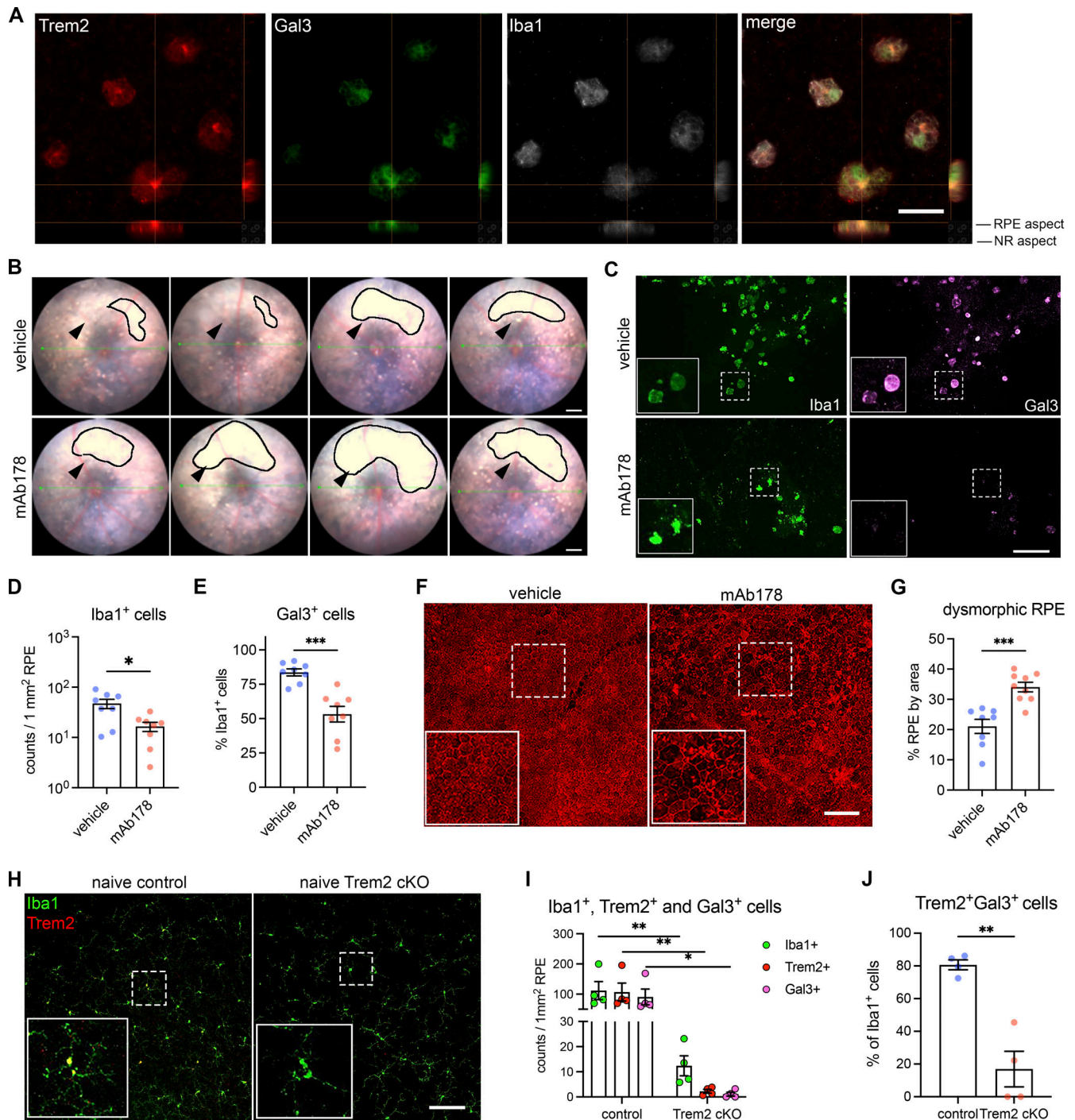


Figure S3. Regulation by Trem2 signaling in subretinal microglia. (A) Split views of confocal scans show the colocalization of Trem2 (red), Gal3 (green), and Iba1 (white) in the subretinal microglia. Lines indicate the RPE-facing and neuroretina (NR)-facing aspects as indicated. Scale bar: 50 μ m. (B) Fundus images show increased subretinal white lesions in anti-Trem2 mAb178-treated mice in LD, as indicated by arrowheads. Images of four individual mice per group are shown. Scale bar: 0.5 mm. (C) Images of Iba1 (green) and Gal3 (magenta) staining in subretinal microglia between control and mAb178-treated mice in LD. Scale bar: 100 μ m. (D and E) Quantifications of Iba1⁺ cells and Gal3⁺ cells between control and mAb178 ($n = 8$ per group). (F) Images of phalloidin staining in RPE flatmounts from control and mAb178-treated mice in LD. Scale bar: 100 μ m. (G) Quantifications of dysmorphic RPE cells between control ($n = 8$) and mAb178- ($n = 9$) treated mice. (H) Images of Iba1 (green) and Trem2 (red) in microglia from the inner retina of naive control and Trem2 cKO mice. Scale bar: 50 μ m. (I) Frequencies of Iba1⁺ cells, Trem2⁺ cells, and Gal3⁺ cells between control and Trem2 cKO mice in LD ($n = 4$ per group). (J) Percentages of Trem2⁺ Gal3⁺ double-positive cells relative to Iba1⁺ cells between control and Trem2 cKO mice in LD ($n = 4$ per group). *: $P < 0.05$; **: $P < 0.01$; ***: $P < 0.001$. Two-way ANOVA with Tukey's post hoc test (I); unpaired Student's t test (D, E, G, I, and J).

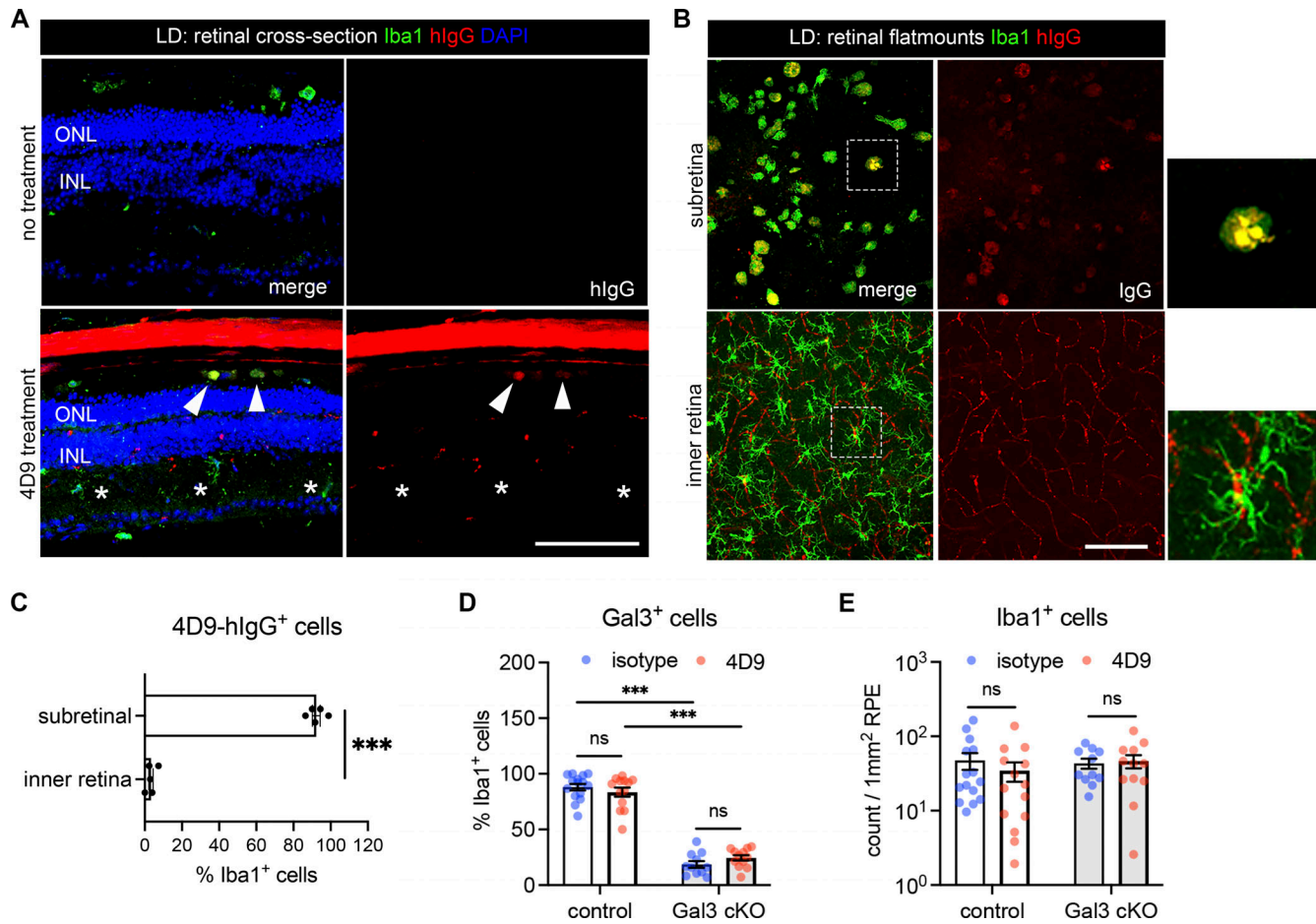


Figure S4. **Subretinal microglia with 4D9 treatment.** (A) Staining of human IgG (red) and Iba1 (green) in retinal cross-sections collected from mice with or without 4D9 treatment in LD. The hlgG is used to trace 4D9 antibodies, which outlines retinal vasculatures in 4D9-treated mice. Arrowheads indicate the presence of 4D9 antibodies in the subretinal microglia, while asterisks indicate the absence of 4D9 antibodies in microglia from the inner retina. INL, inner nuclear layer. (B) Human IgG (red) and Iba1 (green) staining in RPE and neuroretina flatmounts were collected from mice treated with 4D9 antibodies in LD. (C) Quantifications of hlgG⁺ microglia in the subretinal space and neuroretina. (D and E) Quantifications of Iba1⁺ cells and Gal3⁺ cells between control and Gal3 cKO mice treated with either isotype or 4D9 (*n* = 13 per group). Scale bars: 100 μ m. Data were collected from two to four independent experiments. ***: *P* < 0.001; ns: not significant. Unpaired Student's *t* test (C); two-way ANOVA with Tukey's post hoc test (D and E).

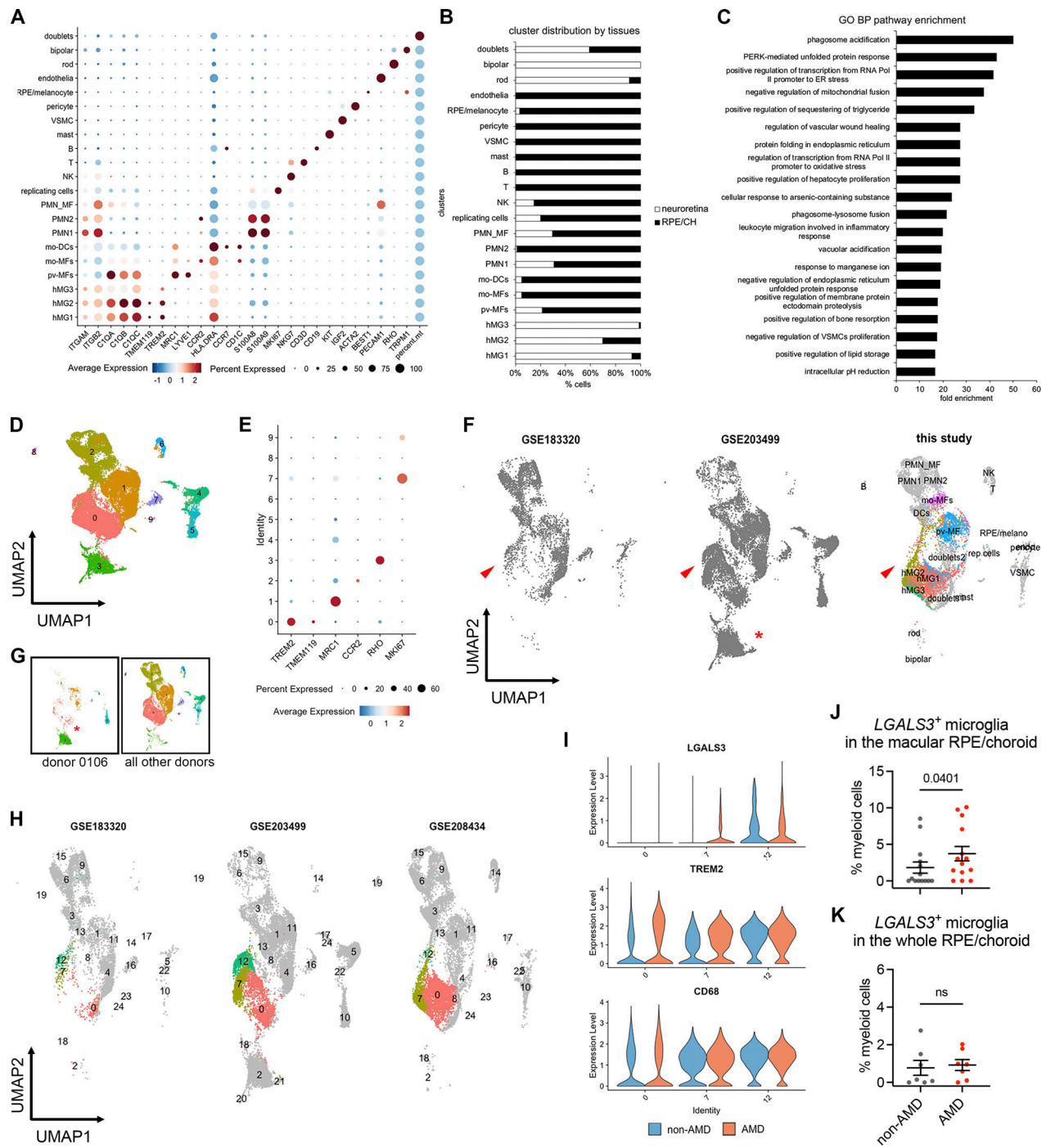


Figure S5. scRNA-seq analysis of myeloid cells from human non-AMD and AMD donors. (A) Marker expression of all human clusters. hMG, human microglia; mo-MFs, monocyte-derived macrophages; pv-MFs, perivascular macrophages; mo-DCs, monocyte-derived dendritic cells; PMN_MF: doublets of polymorphonuclear neutrophils and macrophages; VSMC, vascular smooth muscle cells; NK, natural killer. **(B)** Distribution of clusters by neuroretina and RPE/choroid tissues. The cell number of clusters was normalized to the total counts per tissue. **(C)** Pathway enrichment analysis of subretinal microglia with top 200 shared upregulated genes. The top significant pathways sorted by false discovery and ranked by fold enrichment are shown. GO: Gene Ontology; BP: Biological Process. **(D)** UMAP plot showing integrated clustering analysis of three independent human AMD datasets. Data are shown with low resolution to reveal major cell types. **(E)** Dot plot showing the marker expression of major macrophage clusters. Cluster 3 is enriched with *RHO* expression. **(F)** UMAP plots show the presence of hMG2 cluster in all three scRNA-seq datasets as indicated by arrowheads. **(G)** UMAP plots showing the enrichment of cluster 3 in donor 0106_nAMD. **(H)** UMAP plots showing clustering analysis with high resolution by each dataset and comparable heterogeneity of microglia (cluster 0, 7, and 12). As dataset GSE183320 does not contain neurosensory retina tissues, few cells of major homeostatic microglia (cluster 0) are observed in this dataset. **(I)** Violin plots show the expression of *LGALS3*, *TREM2*, and *CD68* by microglial clusters between non-AMD and AMD donors. Both clusters 7 and 12 show *LGALS3* upregulation as hMG2 cluster identified in this study. **(J and K)** Quantifications of *LGALS3*⁺ microglial clusters (7 and 12) in the macular and whole RPE/choroid tissues between non-AMD and AMD donors. Data were collected from independent datasets and compared using the Mann-Whitney test. P values are shown. ns: not significant.

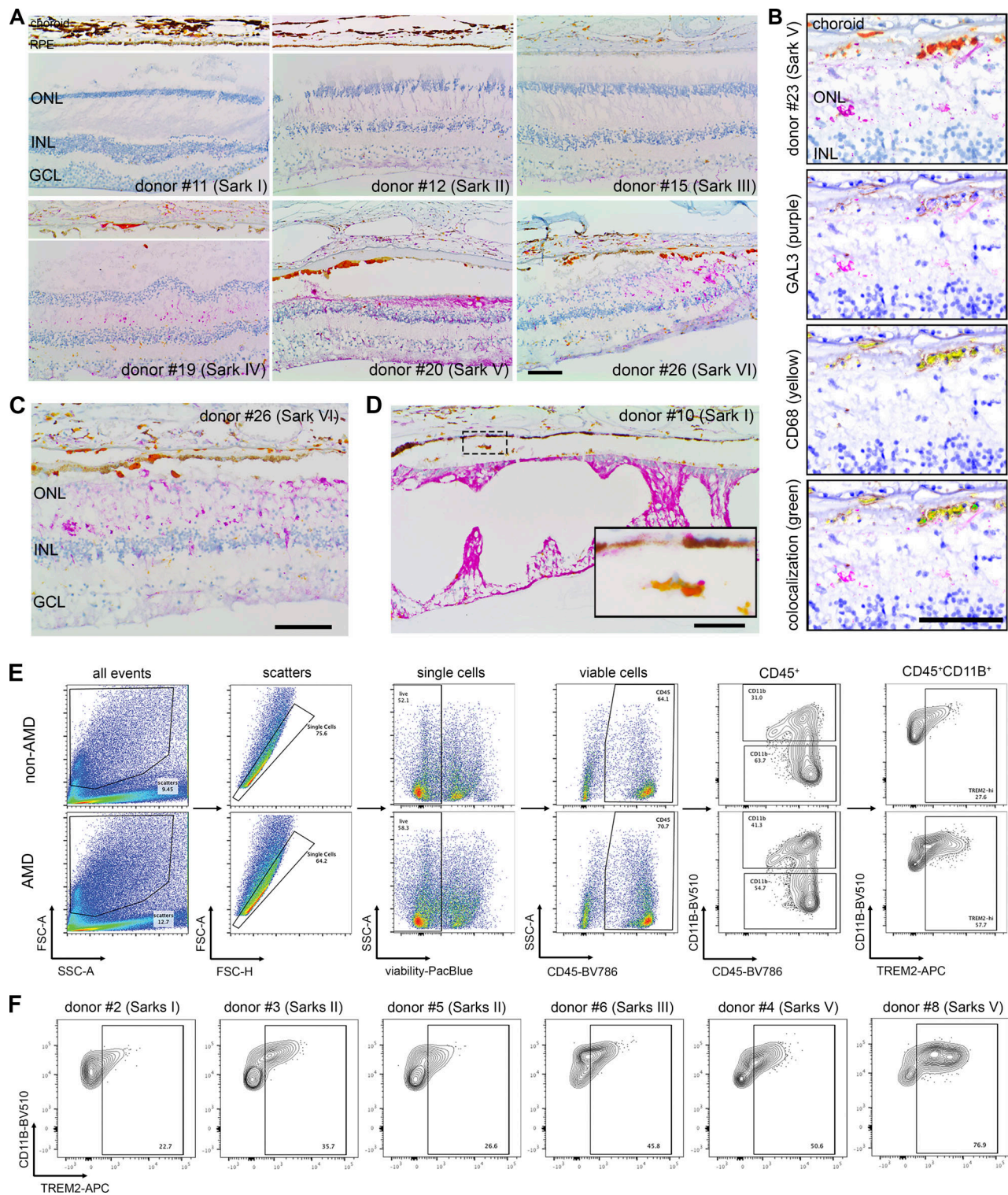


Figure S6. Validation of GAL3 and TREM2 expression by subretinal myeloid cells in human AMD. **(A)** Images of GAL3 (purple) and CD68 (yellow) costaining in the macula region of retinal sections from human donors categorized by Sark grades (I–VI). The macular neurosensory retinas of some subject eyes exhibited fixation-related artifactual detachment. In these subjects, separate images of RPE/choroid tissues are shown. Scale bar: 100 μ m. INL, inner nuclear layer. GCL, ganglion cell layer. **(B)** Spectral imaging of GAL3 and CD68 costaining in the geographic atrophy from donor #23 with advanced AMD (Sarks V). Unmixed purple spectrum (GAL3) and yellow spectrum (CD68) are shown. The areas of colocalized spectra are highlighted in green. Scale bar: 50 μ m. **(C and D)** Images showing the presence of subretinal GAL3 (purple) and CD68 (yellow) double-positive cells in the areas with photoreceptor loss and preserved RPE in the transitional area of the macula from an AMD donor (C) and in the age-related peripheral degeneration of a non-AMD donor (D). Scale bars: 100 μ m. **(E)** Gating strategy of flow cytometry analysis. CD45⁺CD11B⁺ cells and CD45⁺CD11B⁻ cells from control blood were used to determine the gating of TREM2⁺ cells. Concatenated plots are shown for non-AMD and AMD. **(F)** Flow contour plots of individual donors showing an increased percentage of TREM2⁺ myeloid cells in AMD.

Provided online are Table S1, Table S2, and Table S3. Table S1 is the list of shared DEGs of subretinal microglia across mouse models. Table S2 is the metadata of human donors and eye samples. Table S3 is the list of DEGs of three retinal microglial clusters in human donors.